

Accepted Manuscript

Shock capturing for discontinuous Galerkin methods with application to predicting heat transfer in hypersonic flows

Eric J. Ching, Yu Lv, Peter Gnoffo, Michael Barnhardt, Matthias Ihme

PII: S0021-9991(18)30610-7
DOI: <https://doi.org/10.1016/j.jcp.2018.09.016>
Reference: YJCPH 8263

To appear in: *Journal of Computational Physics*

Received date: 3 November 2017
Revised date: 5 September 2018
Accepted date: 8 September 2018

Please cite this article in press as: E.J. Ching et al., Shock capturing for discontinuous Galerkin methods with application to predicting heat transfer in hypersonic flows, *J. Comput. Phys.* (2018), <https://doi.org/10.1016/j.jcp.2018.09.016>

This is a PDF file of an unedited manuscript that has been accepted for publication. As a service to our customers we are providing this early version of the manuscript. The manuscript will undergo copyediting, typesetting, and review of the resulting proof before it is published in its final form. Please note that during the production process errors may be discovered which could affect the content, and all legal disclaimers that apply to the journal pertain.



Highlights

- Developed a robust shock capturing method for DG schemes.
- Intraelement variations are used for shock detection.
- Smooth artificial viscosity is used for shock stabilization.
- Benchmarked heating predictions against FV solvers in hypersonic viscous flows.
- DG predictions exhibit reduced sensitivity to mesh topology and flux functions.

Shock capturing for discontinuous Galerkin methods with application to predicting heat transfer in hypersonic flows

Eric J. Ching^{*,a}, Yu Lv^b, Peter Gnoffo^c, Michael Barnhardt^d, Matthias Ihme^a

^a*Department of Mechanical Engineering, Stanford University, Stanford, CA 94305, USA*

^b*Department of Aerospace Engineering, Mississippi State University, Mississippi State, MS 39762, USA*

^c*NASA Langley Research Center, Hampton, VA 23681, USA*

^d*NASA Ames Research Center, Mountain View, CA 94035, USA*

Abstract

This study is concerned with predicting surface heat transfer in viscous hypersonic flows using high-order discontinuous Galerkin (DG) methods. Currently, finite-volume (FV) schemes are most commonly employed for computing flows in which surface heat transfer is a target quantity; however, these schemes suffer from large sensitivities to a variety of factors, such as the inviscid flux function and the computational mesh. High-order DG methods offer advantages that can mitigate these sensitivities. As such, a simple and robust shock capturing method is developed for DG schemes. The method combines intraelement variations for shock detection with smooth artificial viscosity (AV) for shock stabilization. A parametric study is performed to evaluate the effects of AV on the solution. The shock capturing method is employed to accurately compute double Mach reflection and viscous hypersonic flows over a circular half-cylinder and a double cone, the latter of which involves a complex flow topology with multiple shock interactions and flow separation. Results show this methodology to be significantly less sensitive than FV schemes to mesh topology and inviscid flux function. Furthermore, quantitative comparisons with state-of-the-art FV calculations from an error vs. cost perspective are provided.

Keywords: Discontinuous Galerkin method, Hypersonic flow, Shock capturing, Artificial viscosity, Heat transfer

MCS: 76K05, 76M10, 76J20

1. Introduction

The robust and accurate computation of hypersonic flows is the subject of active research. One of the primary difficulties is correctly predicting surface heat transfer, which exhibits strong sensitivities to shock-induced instabilities, such as the carbuncle phenomenon, and errors that propagate to the thermal

*Corresponding author

Email address: eching@stanford.edu (Eric J. Ching)

boundary layer [1, 2]. Currently, low-order finite-volume (FV) discretizations combined with limiters are most commonly used for such problems [2, 3, 4]. Although these methods have been shown to provide good heating predictions in a variety of hypersonic flow configurations in which the mesh is specifically aligned with strong shocks, results often suffer substantially in the absence of shock-conformed meshes [1]. In recent assessments of standard FV techniques, Kitamura *et al.* [2, 5, 6] found heat transfer predictions, particularly on non-shock-aligned meshes, to be extremely sensitive to a variety of factors, such as the inviscid flux scheme, the choice of reconstructed variables, and the limiter along with associated parameters. Unless the correct combination of the aforementioned factors is selected, large errors are observed in heating predictions, even in cases where thermodynamic quantities are accurately computed and the solution is free from carbuncles. Although generating meshes that are aligned with shocks is straightforward for simpler problems, the geometric and physical complexities typically associated with real hypersonic applications call for solution algorithms that produce good heating results regardless of mesh topology. One promising approach is the multi-dimensional inviscid flux reconstruction procedure [7], which produced good heating results for various hypersonic flow configurations on tetrahedral meshes. Automatic shock fitting techniques provide another potential avenue for resolving the issue of mesh dependence [8, 9].

Apart from FV schemes, an encouraging approach to computing hypersonic flows is finite-element-based discretizations, namely high-order discontinuous Galerkin (DG) methods [10, 11]. This family of numerical methods offers a number of advantages over classical schemes, such as arbitrarily high spatial order of accuracy, geometric flexibility, a high degree of scalability, and compatibility with *hp*-adaptation strategies. DG methods have displayed encouraging performance in the field of steady aerodynamics [12, 13], although they have also shown success in chemically reacting flows [14, 15], turbomachinery applications [16, 17], and turbulent flows [18, 19, 20]. Recent efforts have been dedicated to improving the robustness of high-order approximations of flow-field discontinuities, which commonly lead to nonlinear instabilities and solver divergence. Two essential ingredients for dealing with shocks are shock detection and shock stabilization, both of which have been extensively studied with regard to finite-difference (FD) and FV discretizations. In the context of DG methods, a number of shock detectors have been developed. Persson and Peraire [21] proposed a resolution sensor based on the decay rate of the Fourier modes of the solution approximation. Vuik *et al.* [22] projected the high-order solution onto a multiwavelet basis to identify discontinuous regions, and Krivodonova *et al.* [23] used interelement variable jumps. Recently, the entropy-residual was shown to accurately detect shocks in inviscid flows [24]. A comparison of various shock indicators has been performed by Qiu and Shu [25].

To stabilize discontinuities, one natural approach is to increase the mesh resolution in the detected regions, but this is not always sufficient or feasible. Instead, mesh refinement is typically supplemented or entirely replaced by limiting or artificial viscosity (AV) techniques. Yu *et al.* [26] found that although limiters may be more efficient, they are more likely to dampen small-scale features. In addition, limiters

are difficult to apply to curved elements and to high polynomial approximation orders. These issues are less severe in AV methods, which have seen significant contributions by researchers such as Hartmann [27], Zingan *et al.* [28], and Aliabadi *et al.* [29]. In their classical subcell-resolution methodology, Persson and Peraire [21] proposed adding to troubled cells an elementwise-constant AV that scales with the ratio of local element size to polynomial order. This was extended to RANS calculations by Nguyen *et al.* [30]. Recently, smooth AV formulations have gained popularity since elementwise-constant formulations tend to generate spurious oscillations near the shock as a result of large jumps in AV magnitude among neighboring elements [31, 32]. Most notably, Barter and Darmofal [33] developed an AV formulation in which the artificial viscosity is treated as a state variable governed by a time-dependent diffusion equation. This formulation was shown to be more robust and accurate than conventional elementwise-constant methodologies.

These significant advances in shock capturing methods have enabled the computation of hypersonic problems using DG methods. Many inviscid flows in this regime have been calculated. However, only a limited number of hypersonic viscous flows, particularly those in which the heat transfer load is a target quantity, have been computed. Barter and Darmofal [33] used fourth-order-accurate polynomials to compute hypersonic flow over a circular cylinder with randomly oriented tetrahedra. Despite some small spanwise variations, they obtained good surface heating results. Burgess [34] computed hypersonic flow over a circular cylinder on a quadrilateral mesh and successfully applied *hp*-adaptation techniques, and Brazell and Mavriplis [35] computed hypersonic flow over a sphere. Papoutsakis *et al.* [36] were able to capture key flow structures of chemically reacting flow over a double cone configuration using a second-order-accurate DG discretization, although quantitative comparisons with FV solutions and experimental results revealed a need for improvement. On the whole, however, viscous hypersonic flows remain largely unexplored by DG methods.

In light of the potential for DG schemes to simulate hypersonic flows, the first objective of the present work is to develop a simple and robust shock capturing method suited for viscous high-speed flows. The method uses intraelement variations to detect shocks and employs AV for stabilization. The AV is smoothed by solving a simple linear, elliptic, time-independent partial differential equation. The second objective is to conduct a thorough investigation of the sensitivities of DG schemes combined with the proposed shock capturing formulation to mesh topology, inviscid and viscous flux functions, and the properties of AV added to the domain. Finally, heating predictions are benchmarked against results obtained from a state-of-the-art FV solver widely used for hypersonic applications.

The remainder of the paper is organized as follows: Section 2 outlines the governing equations and DG discretization, followed by a description of the shock capturing formulation in Section 3. The subsequent section focuses on results for three hypersonic test cases: double Mach reflection, flow over a circular half-cylinder, and flow over a double cone. Detailed investigations into the influences of AV, flux functions, and grid-shock alignment on surface heating predictions are performed. The paper concludes with a summary

of the major findings.

2. Mathematical formulation

2.1. Governing Equations

The compressible flow equations describing conservation of mass, momentum, and total energy are given as

$$\partial_t \rho + \nabla \cdot (\rho \mathbf{u}) = 0, \quad (1a)$$

$$\partial_t (\rho \mathbf{u}) + \nabla \cdot (\rho \mathbf{u} \otimes \mathbf{u} + P \mathbf{I}) = \nabla \cdot \boldsymbol{\tau}, \quad (1b)$$

$$\partial_t (\rho e) + \nabla \cdot (\mathbf{u}(\rho e + P)) = \nabla \cdot (\mathbf{u} \cdot \boldsymbol{\tau} - \mathbf{q}), \quad (1c)$$

where ρ is the density, \mathbf{u} is the velocity, P is the pressure, and e is the total energy. The viscous stress tensor and heat flux are specified as

$$\boldsymbol{\tau} = \mu [\nabla \mathbf{u} + (\nabla \mathbf{u})^T] - \frac{2}{3} \mu (\nabla \cdot \mathbf{u}) \mathbf{I}, \quad (2a)$$

$$\mathbf{q} = -\kappa \nabla T, \quad (2b)$$

where μ is the dynamic viscosity, obtained using Sutherland's law for air, and κ is the thermal conductivity, which is related to μ by the Prandtl number, Pr , assumed here to be a constant value of 0.71. This study assumes a calorically perfect gas with a heat capacity ratio, γ , of 1.4. The above set of equations is closed by relating pressure to internal energy via the ideal gas law,

$$P = (\gamma - 1) \left(\rho e - \frac{\rho}{2} \mathbf{u} \cdot \mathbf{u} \right). \quad (3)$$

Note that these simplifications are appropriate for evaluating shock capturing schemes, but more complex gas and transport models are often used for realistic hypersonic applications [37].

2.2. Discontinuous Galerkin Discretization

To develop a DG framework, the governing equations in Eqs. (1) are expressed in vector form as

$$\partial_t \mathbf{U} + \nabla \cdot \mathbf{F} = \nabla \cdot \mathbf{Q}, \quad (4)$$

where $\mathbf{U} \in \mathbb{R}^{N_U}$ is the conservative state vector, $\mathbf{F} \in \mathbb{R}^{N_U \times N_d}$ is the inviscid flux, and $\mathbf{Q} \in \mathbb{R}^{N_U \times N_d}$ is the viscous-diffusive flux, with N_U being the number of state variables and N_d the number of spatial dimensions. \mathbf{F} is a nonlinear function of the full state vector, while \mathbf{Q} can be linearized with respect to the gradients of the state variables [38].

The computational domain Ω is partitioned into a set of N_e nonoverlapping elements $\{\Omega_e\}_{e=1,\dots,N_e}$, with boundaries $\partial\Omega_e$. The finite-dimensional test space \mathcal{V}_h^p is defined as

$$\mathcal{V}_h^p = \{\phi \in L^2(\Omega), \phi^e \equiv \phi|_{\Omega_e} \in \mathcal{P}_p(\Omega_e) \ \forall \ \Omega_e \in \Omega\}, \quad (5)$$

where ϕ is the test function and \mathcal{P}_p denotes the space of polynomial functions of degree p . The global solution \mathbf{U} is approximated by $\mathbf{U} = \bigoplus_{e=1}^{N_e} \mathbf{U}^e$, with the local polynomial approximation given by

$$\mathbf{U}^e(t, \mathbf{x}) = \sum_{n=1}^{N_p} \tilde{\mathbf{U}}_n^e(t) \phi_n^e(\mathbf{x}), \quad (6)$$

where $\tilde{\mathbf{U}}_n^e(t)$ is the n th expansion coefficient, N_p is the number of polynomial coefficients, and ϕ_n are the basis functions, which in this work are chosen to be Lagrange polynomials. Then, letting \mathbf{F} and \mathbf{Q} be the approximations to \mathbf{F} and \mathbf{Q} , respectively, and by multiplying Eq. (4) by ϕ and integrating over the domain, the following general formulation can be obtained: find $\mathbf{U} \in \mathcal{V}_h^p$ such that for $e = 1, \dots, N_e$,

$$\int_{\Omega_e} \phi_m^e \partial_t \mathbf{U}^e d\Omega_e + \int_{\Omega_e} \phi_m^e \nabla \cdot \mathbf{F} d\Omega_e = \int_{\Omega_e} \phi_m^e \nabla \cdot \mathbf{Q} d\Omega_e, \quad (7)$$

for $m = 1, \dots, N_p$. Performing integration by parts on the advection term, the LHS of Eq. (7) can be expressed as

$$\int_{\Omega_e} \phi_m^e \partial_t \mathbf{U}^e d\Omega_e + \int_{\Omega_e} \phi_m^e \nabla \cdot \mathbf{F} d\Omega_e = \int_{\Omega_e} \phi_m^e \partial_t \mathbf{U}^e d\Omega_e - \int_{\Omega_e} \nabla \phi_m^e \cdot \mathbf{F} d\Omega_e + \oint_{\partial\Omega_e} \phi_m^e \mathbf{F} \cdot \hat{\mathbf{n}} d\Gamma_e \quad (8a)$$

$$\approx \sum_{n=1}^{N_p} d_t \tilde{\mathbf{U}}_n^e \int_{\Omega_e} \phi_m^e \phi_n^e d\Omega_e - \int_{\Omega_e} \nabla \phi_m^e \cdot \mathbf{F} d\Omega_e + \oint_{\partial\Omega_e} \phi_m^{e+} \hat{\mathbf{F}} d\Gamma_e, \quad (8b)$$

where $\hat{\mathbf{n}}$ is the outward pointing normal on $\partial\Omega_e$, and the notations $(\cdot)^+$ and $(\cdot)^-$ refer to interior and exterior information about element Ω_e , respectively. The numerical flux $\hat{\mathbf{F}}$ is evaluated via a Riemann solver. In this study, the Riemann solvers employed are the Roe [39], HLLC [40], AUSM+ [41], and SLAU [42] flux functions.

To describe the discretization of the viscous flux, let $\mathbf{Q}_i \in \mathbb{R}^{N_d}$ be the (linearized) diffusion flux of the i th state variable such that

$$\mathbf{Q}_i = \mathcal{D}_i : \nabla \mathbf{U} \quad (9a)$$

$$= \sum_{k=1}^{N_U} \mathcal{D}_{ik} \cdot \nabla U_k \quad (9b)$$

where $\mathcal{D} \in \mathbb{R}^{N_d \times N_d \times N_U \times N_U}$ is a fourth-order tensor representing the first-order differentiation of the viscous flux with respect to the gradient of the state, i.e. $\mathcal{D} = \partial \mathbf{Q} / \partial (\nabla \mathbf{U})$. Since the overall discretization of the diffusion term is distributive over addition, this formulation can be further simplified by first discretizing

$\mathbf{Q}_i^k = \mathcal{D}_{ik} \cdot \nabla U_k$. Note that for each combination of i and k , $\mathbf{Q}_i^k \in \mathbb{R}^{N_d}$, $\mathcal{D}_{ik} \in \mathbb{R}^{N_d \times N_d}$, and $\nabla U_k \in \mathbb{R}^{N_d}$. Noting that $\nabla \phi_m^e \cdot (\mathcal{D}_{ik} \cdot \nabla U_k) = \nabla U_k \cdot (\mathcal{D}_{ik}^T \cdot \nabla \phi_m^e)$, the local discretization of $\nabla \cdot \mathbf{Q}_i^k$ is as follows:

$$\int_{\Omega_e} \phi_m^e \nabla \cdot \mathbf{Q}_i^k d\Omega_e = - \int_{\Omega_e} \nabla \phi_m^e \cdot (\mathcal{D}_{ik} \cdot \nabla U_k) d\Omega_e + \oint_{\partial\Omega_e} \phi_m^e \mathbf{Q}_i^k \cdot \hat{\mathbf{n}} d\Gamma_e \quad (10a)$$

$$= \int_{\Omega_e} U_k \nabla \cdot (\mathcal{D}_{ik}^T \cdot \nabla \phi_m^e) d\Omega_e - \oint_{\partial\Omega_e} U_k (\mathcal{D}_{ik}^T \cdot \nabla \phi_m^e) \cdot \hat{\mathbf{n}} d\Gamma_e + \oint_{\partial\Omega_e} \phi_m^e \mathbf{Q}_i^k \cdot \hat{\mathbf{n}} d\Gamma_e \quad (10b)$$

$$\approx \int_{\Omega_e} U_k \nabla \cdot (\mathcal{D}_{ik}^T \cdot \nabla \phi_m^e) d\Omega_e - \oint_{\partial\Omega_e} \hat{U}_k (\mathcal{D}_{ik}^T \cdot \nabla \phi_m^e)^+ \cdot \hat{\mathbf{n}} d\Gamma_e + \oint_{\partial\Omega_e} \phi_m^{e+} \hat{Q}_i^k d\Gamma_e \quad (10c)$$

$$= - \int_{\Omega_e} \nabla \phi_m^e \cdot (\mathcal{D}_{ik} \cdot \nabla U_k) d\Omega_e + \oint_{\partial\Omega_e} (U_k^+ - \hat{U}_k) (\mathcal{D}_{ik}^T \cdot \nabla \phi_m^e)^+ \cdot \hat{\mathbf{n}} d\Gamma_e + \oint_{\partial\Omega_e} \phi_m^{e+} \hat{Q}_i^k d\Gamma_e. \quad (10d)$$

The three terms from left to right on the RHS of Eq. (10d) represent interior diffusion, dual consistency, and interelement viscous effects. The RHS of Eq. (7) is then given by

$$\int_{\Omega_e} \phi_m^e \nabla \cdot \mathbf{Q}_i d\Omega_e = \sum_{k=1}^{N_U} \int_{\Omega_e} \phi_m^e \nabla \cdot \mathbf{Q}_i^k d\Omega_e, \quad (11)$$

in which the RHS is evaluated from Eq. (10d). In this study, $\hat{U} = \{U\}$, where the operator $\{\cdot\} := \frac{1}{2}[(\cdot)^+ + (\cdot)^-]$ is the mean value across element faces, and the prescription of \hat{Q}_i follows either the interior penalty (IP) scheme [43] or the second form of Bassi and Rebay (BR2) [38].

All integrals in Eqs. (8b) and (10d) are evaluated using Gaussian quadrature with an order of accuracy no less than $2p + 1$.

3. Shock Capturing Method

This section introduces the shock capturing framework and describes how AV is localized, smoothed, and added to the governing equations. The method builds upon ideas from the work of Barter and Darmofal [33], and important differences are discussed. Each component of the shock capturing method is straightforward and easy to implement.

3.1. Artificial viscosity formulation

To regularize the system near discontinuities, an AV term, $\nabla \cdot \mathbf{Q}_{AV}$, is added to the RHS of Eq. (4), with $\mathbf{Q}_{AV,i} \in \mathbb{R}^{N_U}$ defined as [21, 33]

$$\mathbf{Q}_{AV,i} = \sum_{j=1}^{N_d} \eta \frac{h_{ij}}{h} \frac{\partial \mathbf{U}^*}{\partial x_j}, \quad (12)$$

where $\mathbf{U}^* = [\rho, \rho \mathbf{u}, \rho h]^T$ is the modified state vector, with $h = e + p/\rho$ the total enthalpy, which yields better preservation of total enthalpy across a shock in the steady, inviscid limit [33]. η is the spatially-dependent AV, $\mathbf{h} \in \mathbb{R}^{N_d \times N_d}$ is a measure of the local element size that should be smooth and take into account mesh

anisotropy, and \bar{h} is a volume-based length scale. For evaluating \mathbf{h} , this work uses the smooth Riemannian metric tensor field [44, 45], which provides an axis-independent measure of local length scales that better accounts for anisotropy than the element bounding boxes used by Barter and Darmofal [33].

To localize the AV around discontinuities, a shock indicator is required to detect troubled elements. Barter and Darmofal employed pressure jumps across element faces as well as the resolution sensor of Persson and Peraire [21] to detect discontinuities [33]. This work uses a sensor based on intraelement variations, defined as

$$S_e = \sqrt{\frac{\int_{\Omega_e} (\xi/\bar{\xi} - 1)^2 d\Omega}{|\Omega_e|}}, \quad (13)$$

where ξ is chosen in this work to be pressure, as defined in Eq. (3), and $\bar{\xi}$ denotes its average over Ω_e . This shock sensor is small in smooth flow regions and assumes larger values in the vicinity of discontinuities. It is straightforward to implement, and information from neighboring elements is not required.

Before obtaining the appropriate form for use in Eq. (12), the AV is first applied in an elementwise-constant manner as

$$\eta_0^e = C_\eta \lambda_{\max} \frac{\bar{h}}{\max(1, p)} \bar{S}_e, \quad (14)$$

where C_η is a scaling factor, λ_{\max} is the maximum wave speed in the element, and the \bar{h}/p -scaling introduced by Persson and Peraire [21] has been incorporated. \bar{S}_e is a smooth scaling of the sensor given as

$$\bar{S}_e(S_e) = \begin{cases} 0, & S < S^* - \Delta S, \\ S, & S > S^* + \Delta S, \\ \frac{S}{2} \left[1 + \sin\left(\frac{\pi}{2\Delta S}(S - S^*)\right) \right], & S^* - \Delta S \leq S \leq S^* + \Delta S, \end{cases} \quad (15)$$

where S^* is a threshold parameter that controls the number of troubled elements flagged by the shock detector. This study found $S^* = 0.125$ and $\Delta S = 0.025$ to be reliable values.

Previous works have shown smooth AV fields to increase robustness and decrease shock-induced errors compared to traditional elementwise-constant AV fields [32, 31, 33]. Therefore, to smooth the elementwise-constant viscosity obtained by Eq. (14), the following elliptic partial differential equation (PDE) is solved for η_s :

$$\eta_s - \nabla \cdot [C_\Delta \Delta]^2 \nabla \eta_s = \eta_0, \quad (16)$$

The Green's function of Eq. (16) corresponds to the filter kernel of Germano used in large eddy simulations of turbulent flows [46]. η_0 is the elementwise-constant AV from Eq. (14), and η_s is the resulting smooth AV. Δ must be an appropriate length scale, in this study chosen to be the local element size \bar{h} , and C_Δ is a parameter that represents a characteristic number of neighboring elements to which the AV will be smoothed. If C_Δ is too small, then the AV field will not be sufficiently smooth, but if it is too large, then the bulk of the AV will no longer be localized to troubled elements. In both cases, large errors may be introduced into

the solution. Note that for $C_\Delta = 1/24$, η_s is a first-order approximation of the output of η_0 passed through a Gaussian filter of length Δ [46]. For illustration, Figure 1 displays a representative elementwise-constant η_0 -field and the resulting smooth η_s -field for hypersonic flow over a circular half-cylinder at a free-stream Mach number of 17.6. Note that the larger amount of artificial viscosity at the outflow boundary is a consequence of the larger element size and the stronger grid-shock misalignment at this region. As a result of the misalignment, the grid is less able to sharply represent the shock, and the shock extent is more likely to be smeared across multiple elements.

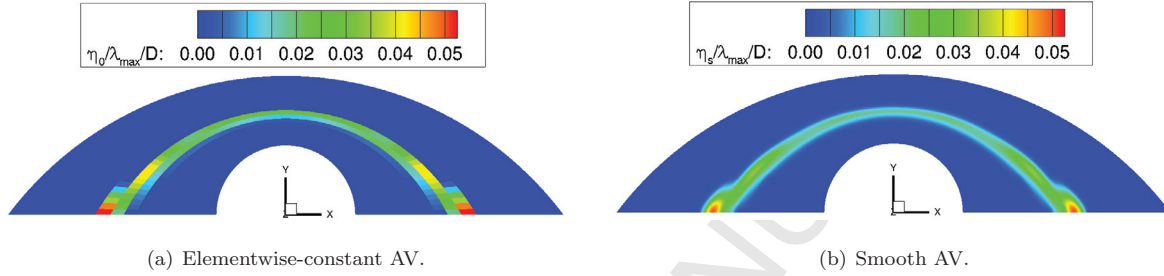


Figure 1: Representative elementwise-constant η_0 -field and the resulting smooth η_s -field after solving Eq. (16) for hypersonic flow over a circular cylinder at a free-stream Mach number of 17.6. D is the cylinder diameter. The flow is from top to bottom.

Equation (16) is solved using a DG discretization in which the solution is approximated using the same basis functions as those used for the approximation of the flow field solution, i.e., $\eta_s^e(t, \mathbf{x}) \approx \sum_{n=1}^{N_p} \tilde{\eta}_{s,n}^e(t) \phi_n^e(\mathbf{x})$. This equation is similar to the PDE employed by Barter and Darmofal [33]; however, they included the unsteady term, considered the AV as a state variable, and evolved the AV in time approximately as fast as the primary state variables. Under their framework, guaranteeing sufficient smoothness of the AV field can result in a very stiff overall system. In the proposed method, the AV is treated separately from the primary state variables. This not only helps to circumvent stiffness issues but also offers greater flexibility in solving Eq. (16). For instance, different tolerances and solution procedures can be applied to Eq. (16), especially since it is in general much easier to solve than the primary governing equations.

It is well-established that boundary layer predictions are very sensitive to excessive numerical dissipation [47]. Therefore, in solving Eq. (16), homogeneous Dirichlet boundary conditions are employed at no-slip walls to decrease the amount of AV added to the boundary layer. Although flow-field discontinuities may occur at walls, the mesh is typically very fine, and if η_0 is nonzero at a boundary element, then η_s will likely be nonzero in nearby elements. Homogeneous Neumann boundary conditions are applied at inflow, outflow, symmetry, and inviscid-wall boundaries. Barter and Darmofal used a Robin boundary condition for all boundaries, but this can still result in large amounts of AV in boundary layers.

The smoothing procedure causes small amounts of AV to be added to elements far away from troubled regions. This is especially problematic when strong shocks are present in the domain that require large

amounts of AV to be stabilized. Furthermore, as previously mentioned, the amount of AV present in boundary layers should be minimized. Therefore, η_s is filtered in order to smoothly clip away values below some lower bound [21, 33] using the following expression:

$$\eta(\eta_s) = \begin{cases} 0, & \eta_s \leq \eta_L, \\ 0.5\eta_H \left[1 + \sin \left(\frac{\pi}{2} \frac{2\eta_s - (\eta_H + \eta_L)}{\eta_H - \eta_L} \right) \right], & \eta_s > \eta_L, \end{cases} \quad (17)$$

where η_H and η_L are the user-prescribed upper and lower bounds, respectively, on η_s . In this study, η_H is set to be the maximum between η_s and $\lambda_{\max} \frac{\bar{h}}{\max(1,p)}$ over each element, and $\eta_L = 0.01\eta_H$. Eq. (17) gives the final value of η used in Eq. (12).

This shock capturing method is compatible with both explicit and implicit time stepping schemes due to the fast residual convergence of Eq. (16). To reduce computational time, the η_s -field from the previous time step can be used as the initial condition for the current time step. Furthermore, the AV field may be frozen over a time span during which flow-field discontinuities do not change significantly. In this study, which employs implicit time stepping, the AV is considered to be weakly coupled to the state variables, i.e., $\partial \mathbf{Q}_{AV} / \partial \mathbf{U} = 0$. This is not expected to affect the computed solutions, and it substantially reduces the implementation challenges associated with linearization [32].

For simulations of steady-state flows, small-scale oscillations in the flow field that induce slight changes in the AV fields generated at each time step can cause stalling of residuals. Nevertheless, this typically only occurs once the residual has already decreased several orders of magnitude and does not influence aerothermodynamic quantities of interest. This is also commonly observed in finite-volume simulations of hypersonic flows [48].

4. Results

This section discusses results for three test cases: the double Mach reflection problem, hypersonic flow over a circular half-cylinder, and hypersonic flow over a double cone. The first test case is a transient inviscid flow problem while the latter two are steady-state viscous flow problems in which accurate surface heating is difficult to predict.

4.1. Double Mach reflection

Introduced by Woodward and Collela [49], this two-dimensional inviscid flow configuration consists of a Mach-10 shock impinging on a 30° wedge. It involves a complex shock structure that features two triple points and multiple shocks of different orientations. A reliable indicator of solution quality is the prediction of Kelvin-Helmholtz instability along the shear layer emanating from the primary triple point. The

computational domain is $[0, 4] \times [0, 1]$, partitioned with uniform quadrilateral elements. The post-shock and pre-shock states at time t are given by

$$[\rho, u, v, P] = \begin{cases} [8, 8.25 \cos(\frac{\pi}{6}), -8.25 \sin(\frac{\pi}{6}), 116.5], & x < x_0 + \frac{y}{\sqrt{3}} + \frac{2u_s t}{\sqrt{3}}, \\ [1.4, 0, 0, 1.0], & x \geq x_0 + \frac{y}{\sqrt{3}} + \frac{2u_s t}{\sqrt{3}}, \end{cases} \quad (18)$$

where $x_0 = 1/6$ and $u_s = 10$ is the shock speed. Eq. (18) is used to specify both the initial conditions and the conditions along the top boundary of the domain. Post-shock conditions are prescribed on the left boundary as well as on the region $x \in [0, x_0]$ along the bottom boundary. The remainder of the bottom boundary is set to inviscid-wall conditions, and extrapolation is employed at the right boundary. In all simulations considered here, the final time is $t = 0.2$, the polynomial order is $p = 2$, and the time-stepping scheme is third-order backward differencing.

The density field for a mesh with 960×240 elements is shown in Figure 2. All flow-field discontinuities are well-captured. A zoom-in on the shear layer and wall jet illustrates sharp wave fronts and good prediction of Kelvin-Helmholtz instabilities. To examine the influence of the AV on the solution, a parametric study was performed on a coarser mesh with 480×120 elements. The AV profile can be characterized by its *magnitude* and *span*, which are controlled by C_η (Eq. (14)) and C_Δ (Eq. (16)), respectively. The values of C_η and C_Δ for each case are listed in Table 1.

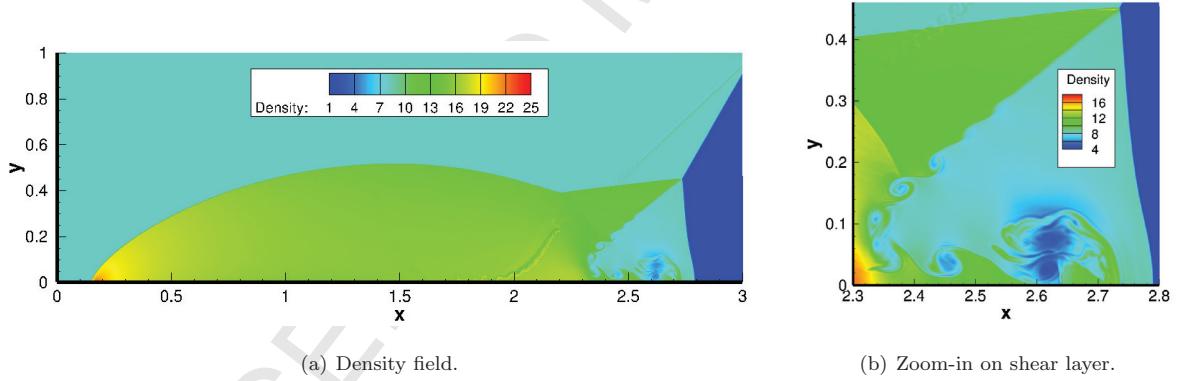


Figure 2: Simulation of double Mach reflection on a regular domain with 960×240 quadrilateral elements. Results were obtained at $t = 2$ with a polynomial order of $p = 2$ and third-order backward differencing in time. The AV parameters were $C_\eta = 0.25$ and $C_\Delta = 0.1$.

The density and AV fields for each case are displayed in Figure 3. In all cases, the artificial viscosity is concentrated around the incident shock, the Mach stem, and the elongated bow shock. In cases 2 and 4, the AV is somewhat higher than in case 1, whereas in cases 3 and 5, the AV is significantly higher. The influences of the AV are more distinct in Figure 4, which provides the density fields zoomed in on the shear layer. Case 1 gives slightly better prediction of the flow topology than cases 2 and 4. On the other

Table 1: AV parameters for parametric study of effects of *magnitude* and *span* of AV on the solution to double Mach reflection.

Case	C_η	C_Δ
1	0.25	0.1
2	0.5	0.1
3	2.0	0.1
4	0.5	0.25
5	3.0	1.0

hand, the excessive AV in cases 3 and 5 results in considerable dissipation and hampers the development of hydrodynamic instability. These results suggest that solution quality is relatively insensitive to the amount of AV added to the domain provided that the AV is not exceedingly large (as in cases 3 and 5).

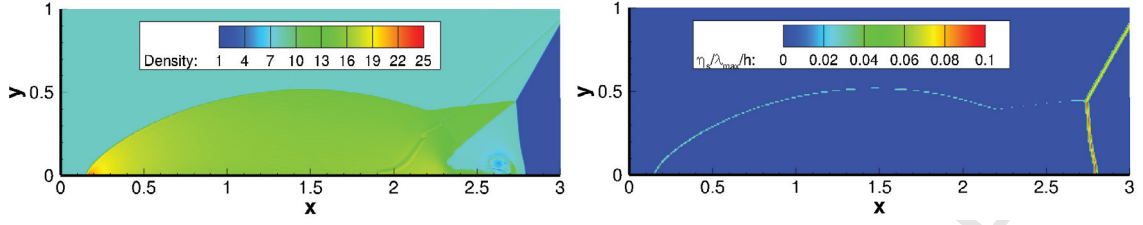
4.2. Viscous hypersonic test cases

The viscous test cases considered in this study are hypersonic flows over a circular half-cylinder and a double cone. The flow parameters investigated here yield steady-state conditions. Meshes with second-order curved elements are used for all simulations. Pseudo-time-stepping is used to facilitate convergence, and GMRES is used to solve the linear system at each time step. In addition, polynomial order sequencing is employed, in which low-order solutions are used as initial conditions to compute higher-order solutions. The intermediate solutions need not be fully converged before projecting to higher orders. Some difficulties may arise when using a $p = 0$ solution to initialize a $p = 1$ calculation. Given that the $p = 0$ solution does not vary within each element, the intraelement-variation shock sensor (Eq. (13)) will not initially flag any troubled elements, giving rise to instabilities in the $p = 1$ calculation. To counteract this, an AV field is generated from the $p = 0$ solution based on an interelement-jump shock sensor (note that interelement jumps are very simple to compute for a $p = 0$ solution). The AV field is frozen to allow the $p = 1$ calculation to evolve for several time steps before reverting to the intraelement-variation shock sensor. Furthermore, computing the $p = 0$ solution with some artificial viscosity added to the domain can reduce the magnitude of interelement fluctuations that may otherwise give rise to large instabilities during the $p = 1$ calculation.

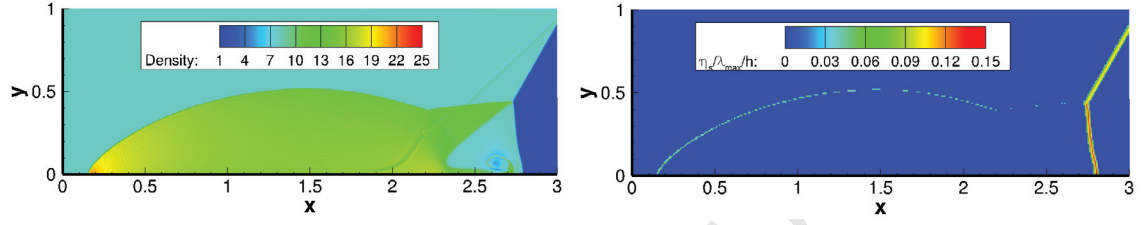
In the simulations considered here, the target quantity is the heat flux along the surface of the body, which is set to be an isothermal no-slip wall. For heat flux evaluations, the temperature gradient can be computed in different ways. One method is to linearize with respect to the state variables as

$$\nabla T = \sum_{j=1}^{N_U} \frac{\partial T}{\partial U_j} \nabla U_j. \quad (19)$$

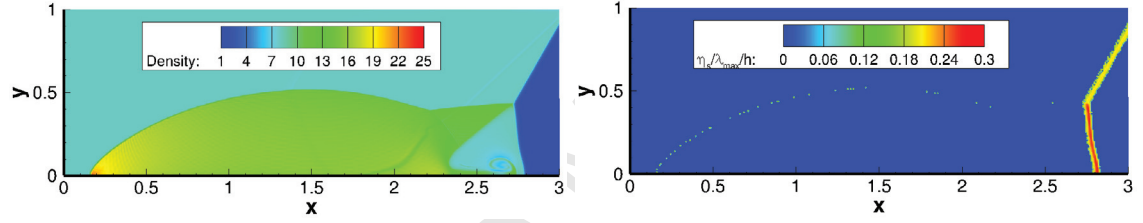
Another method is to compute it based on the following variational formulation for all elements along the



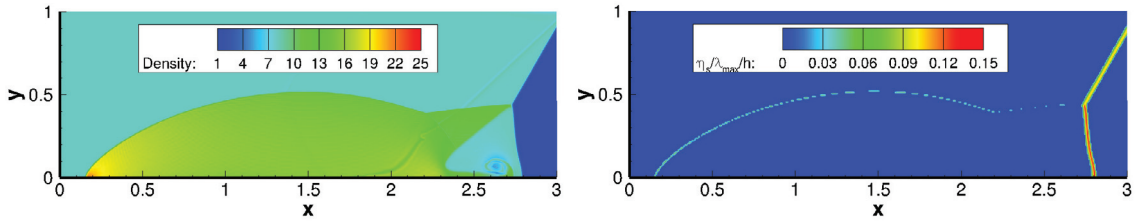
(a) Density and AV fields for case 1 ($C_\eta = 0.25, C_\Delta = 0.1$).



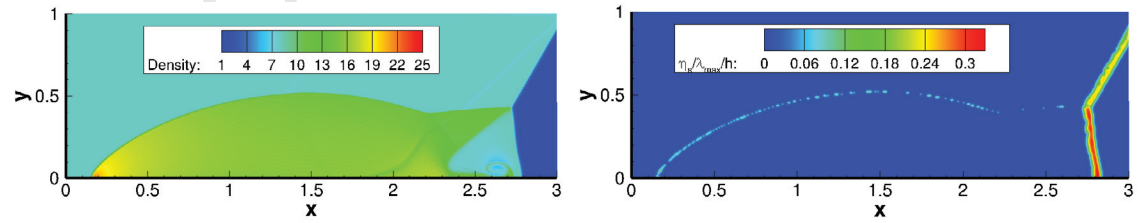
(b) Density and AV fields for case 2 ($C_\eta = 0.5, C_\Delta = 0.1$).



(c) Density and AV fields for case 3 ($C_\eta = 2.0, C_\Delta = 0.1$).

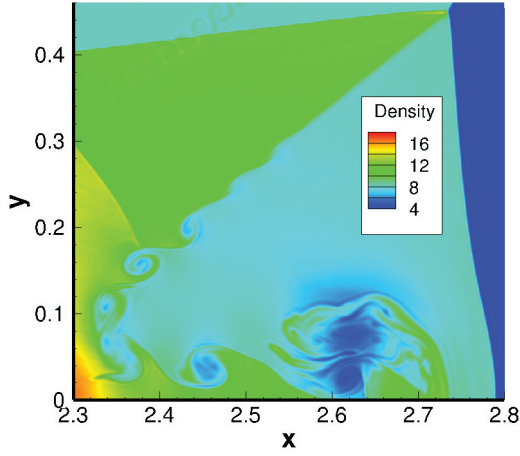


(d) Density and AV fields for case 4 ($C_\eta = 0.5, C_\Delta = 0.25$).

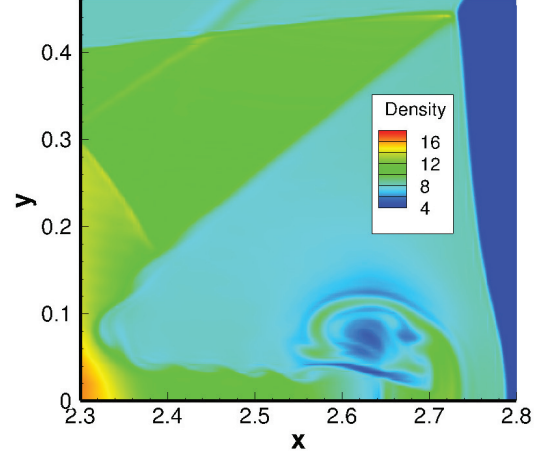


(e) Density and AV fields for case 5 ($C_\eta = 3.0, C_\Delta = 1.0$).

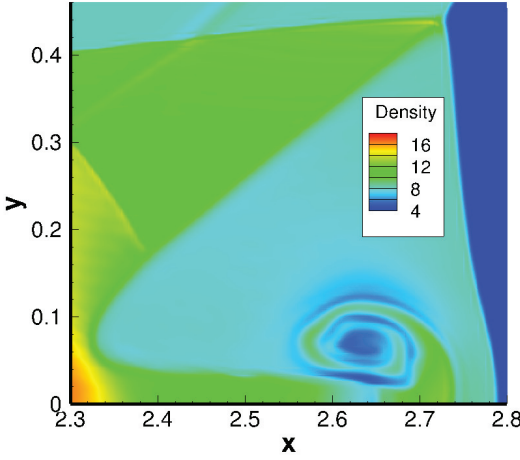
Figure 3: Simulation of double Mach reflection for different values of C_η and C_Δ , as listed in Table 1. The simulations were performed on a regular domain with 480×120 quadrilateral elements. Results were obtained at $t = 0.2$ with a polynomial order of $p = 2$ and third-order backward differencing in time.



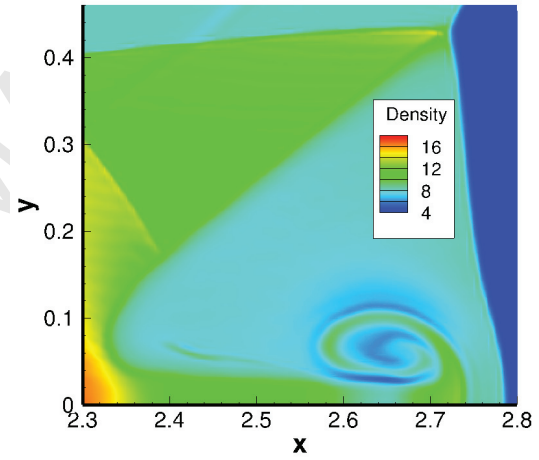
(a) Density field on 960×240 mesh ($C_\eta = 0.25, C_\Delta = 0.1$).



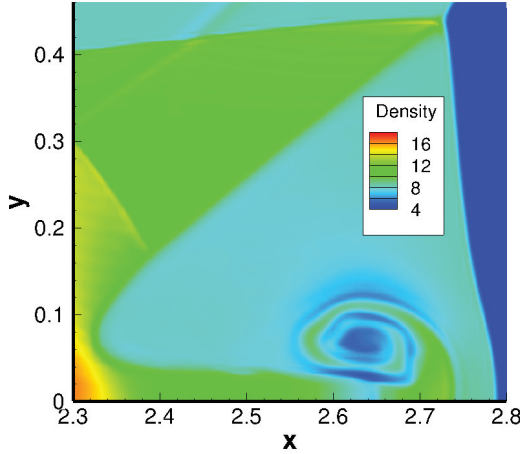
(b) Density field on 480×120 mesh - case 1 ($C_\eta = 0.25, C_\Delta = 0.1$).



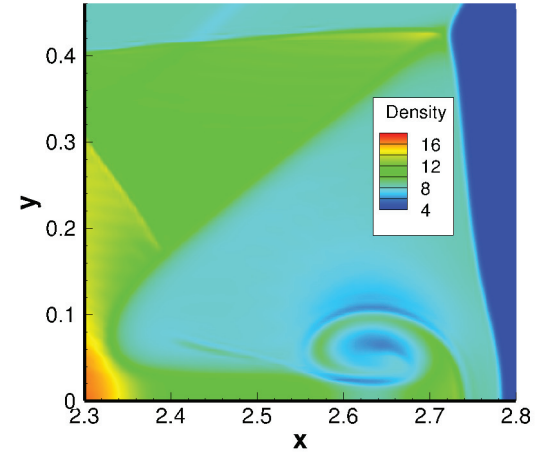
(c) Density field on 480×120 mesh - case 2 ($C_\eta = 0.5, C_\Delta = 0.1$).



(d) Density field on 480×120 mesh - case 3 ($C_\eta = 2.0, C_\Delta = 0.1$).



(e) Density field on 480×120 mesh - case 4 ($C_\eta = 0.5, C_\Delta = 0.25$).



(f) Density field on 480×120 mesh - case 5 ($C_\eta = 3.0, C_\Delta = 1.0$).

Figure 4: Zoom-in on density fields for simulations of double Mach reflection. Results were obtained at $t = 0.2$ with a polynomial order of $p = 2$ and third-order backward differencing in time.

wall:

$$\int_{\Omega_e} \nabla T \cdot \phi^e d\Omega_e = \oint_{\partial\Omega_e} T_{\text{wall}} \phi^e \cdot \hat{\mathbf{n}} d\Gamma_e - \int_{\Omega_e} T \nabla \cdot \phi^e d\Omega_e, \quad (20)$$

where $\phi \in \mathbb{R}^{N_d}$ is a vector of test functions. The wall heat flux is then computed from the wall temperature gradient as $q_{\text{wall}} = -\kappa \nabla T_{\text{wall}} \cdot \hat{\mathbf{n}}$. Additional phenomena, such as surface chemistry and radiation, that often contribute to surface heat transfer in hypersonic applications are not considered here. Note that for $p = 0$ calculations, Eq. (19) gives $q_{\text{wall}} = 0$. For $p \geq 1$, both methods generate nearly identical results. In this study, the heat transfer results are presented nondimensionally via the Stanton number, defined as

$$\text{St} = \frac{q_{\text{wall}}}{c_p \rho_{\infty} |\mathbf{u}|_{\infty} (T_{t,\infty} - T_{\text{wall}})}, \quad (21)$$

where c_p is the specific heat at constant pressure, T_t is the stagnation temperature, and $(\cdot)_{\infty}$ denotes free-stream values.

4.2.1. Hypersonic flow over a circular half-cylinder

The simple geometry and quasi-2D nature of this flow configuration makes it a common benchmark case for assessing the performance of numerical methods and solution algorithms in hypersonic flow predictions [50, 51, 3, 52, 7, 33, 6]. Major challenges are associated with capturing the very strong bow shock and resolving the extremely thin boundary layer. Small inconsistencies in the heat flux profile among various solution methods have been observed. For instance, Gnoffo and White [3] predict a stagnation point Stanton number of 0.0085, Kitamura et al. [6] report a stagnation Stanton number of 0.0076, and Barter and Darmofal [33] predict 0.0082. Overall, there was found to be within 15% variation in the heat flux profile across these calculations.

This test case was found to be extremely mesh-sensitive in FV discretizations. Nompelis *et al.* [50] investigated this problem using a series of meshes with hexahedral elements in the boundary layer, but different element types and sizes in the shock region. Perfectly symmetric heating results were obtained on well-aligned hexahedral elements, but randomly oriented isotropic tetrahedra in the shock region produced large spanwise and circumferential variations in the wall heat flux profile. Higher resolution near the shock moderately improved the results, but asymmetries were still present. Similarly, Gnoffo and White [51] used uniformly biased tetrahedral elements throughout the entire computational domain and observed even larger asymmetries in the heating results. It was only after a series of algorithmic developments culminating in a multidimensional inviscid flux reconstruction procedure [3, 52, 7] that good heating predictions were obtained, despite slight asymmetries still appearing and an increase in the computational cost by a factor of two.

Kitamura *et al.* [6] also computed this flow using an FV discretization on a non-shock-aligned quadrilateral mesh with second-order MUSCL reconstruction [53], central differencing for the viscous flux, the Van Albada limiter [54], and different inviscid flux functions. Wildly varying heat flux profiles were obtained for

the different inviscid flux functions, illustrating the sensitivities of hypersonic heating predictions in a FV framework.

Using a DG discretization, Barter and Darmofal [33] obtained good heating predictions on a mesh with structured tetrahedral elements in the boundary layer and of random orientation outside the boundary layer. Some variations near the stagnation point and spurious oscillations near the outflow boundaries were present. In their AV methodology, the AV is appended to the state vector and a diffusion equation driven by the shock sensor is added to the governing equations. A third-order polynomial approximation was used in conjunction with the Roe and BR2 schemes for the inviscid and viscous fluxes.

The focus of the present study is to evaluate the sensitivities of this type of flow to the AV parameters, the inviscid and viscous flux functions, and mesh topology, in particular a uniformly biased tetrahedral mesh. Furthermore, error-cost comparisons with a state-of-the-art FV solver are provided. The flow parameters for the configuration investigated here are listed in Table 2. Inflow boundary conditions for the entire state vector are specified, extrapolation is used for the outflow boundary conditions, and for three-dimensional calculations, symmetry is employed at extruded boundaries. The surface of the cylinder, with diameter D , is prescribed by an isothermal no-slip wall.

Table 2: Flow parameters for hypersonic flow over circular cylinder. Ma is the Mach number, Re is the Reynolds number based on the cylinder radius, T_{wall} is the cylinder wall temperature, and T_{∞} is the free-stream temperature.

Ma	Re	T_{wall} (K)	T_{∞} (K)
17.605	376,930	500	200

4.2.1.1 Convergence study for 2D mesh

This section investigates the mesh convergence of this calculation at polynomial orders between $p = 1$ and $p = 3$. Two 2D quadrilateral meshes of different resolution (*coarse* and *fine*) were generated without any special consideration to align elements with the bow shock. The coarse mesh consists of 20 elements in the radial direction and 11 elements in the circumferential direction. To create this mesh, an initial linear mesh with 40 elements in the radial direction and 22 elements in the circumferential direction was first generated in GMSH [55]. To achieve quadratic order, groups of linear elements were combined to form individual quadratic elements. The coarse mesh was uniformly refined to generate the fine mesh, resulting in 40 and 22 elements in the radial and circumferential directions, respectively. Both meshes are displayed in Figure 5. The total number of degrees of freedom per state variable is given by $N_e \times (p + 1)^2$. Table 3 summarizes the number of elements, degrees of freedom, and calculated stagnation-point Stanton number for each mesh.

Figure 6 shows the heat flux profiles for the coarse and fine meshes with $p = 1$, $p = 2$, and $p = 3$.

Table 3: Information regarding the quadrilateral meshes used for computing hypersonic flow over a circular cylinder. The number of degrees of freedom (per state variable) is calculated by $N_e \times (p+1)^2$, where p is the polynomial order. The Stanton number is reported at the stagnation point.

Mesh	Element type	No. elements (radial \times azimuthal)	No. degrees of freedom			Stagnation-point Stanton number ($\times 10^3$)		
			$p = 1$	$p = 2$	$p = 3$	$p = 1$	$p = 2$	$p = 3$
Coarse	Quadrilaterals	20×11	880	1980	3520	7.96	8.02	8.08
Fine	Quadrilaterals	40×22	3520	7920	14080	7.98	8.13	8.15

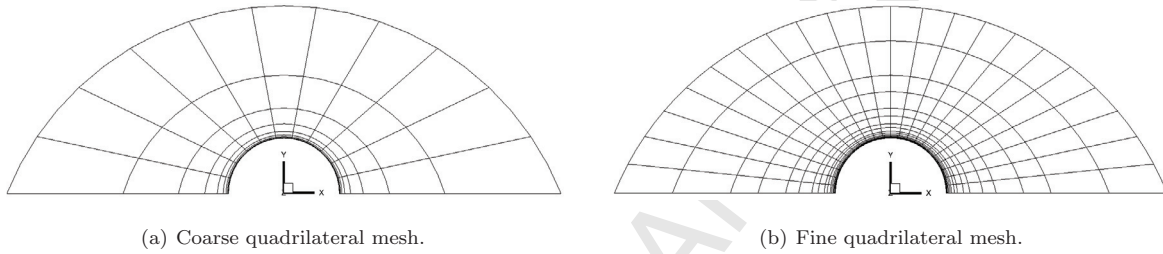


Figure 5: 2D quadrilateral meshes used for hypersonic flow over a circular cylinder. The coarse mesh was uniformly refined to generate the fine mesh.

Each point in Figure 6 represents the heat flux at the center of the corresponding face on the cylinder wall. A reference solution was computed using $p = 3$ on a mesh with twice the resolution of the fine mesh. The stagnation-point Stanton number of the reference solution is 0.00815, which agrees very well with the prediction by Barter and Darmofal [33]. For both meshes, the $p = 2$ and $p = 3$ solutions give nearly exact heating profiles with the reference solution. Note that even with fewer degrees of freedom, the coarse $p = 2$ solution agrees more closely with the reference solution than the fine $p = 1$ solution. This illustrates the benefits of high-order accuracy even for shock-dominated flows.

4.2.1.2 Solution sensitivity to artificial viscosity

This section aims to characterize the effects of AV on the flow field and on surface heating predictions. Similar to what was done for the double Mach reflection test case, a parametric study with varying C_η and C_Δ was performed on the fine $p = 3$ calculation. Five sample cases were examined, with the values of each parameter displayed in Table 4. Case 1 entails a relatively small amount of AV, cases 2 and 4 moderately increase the AV, and cases 3 and 5 significantly increase the AV.

The heat-flux profiles for all five cases are plotted in Figure 7. Despite large differences in the respective AV profiles, only small changes in heat flux are observed. Further insight can be gained by examining the

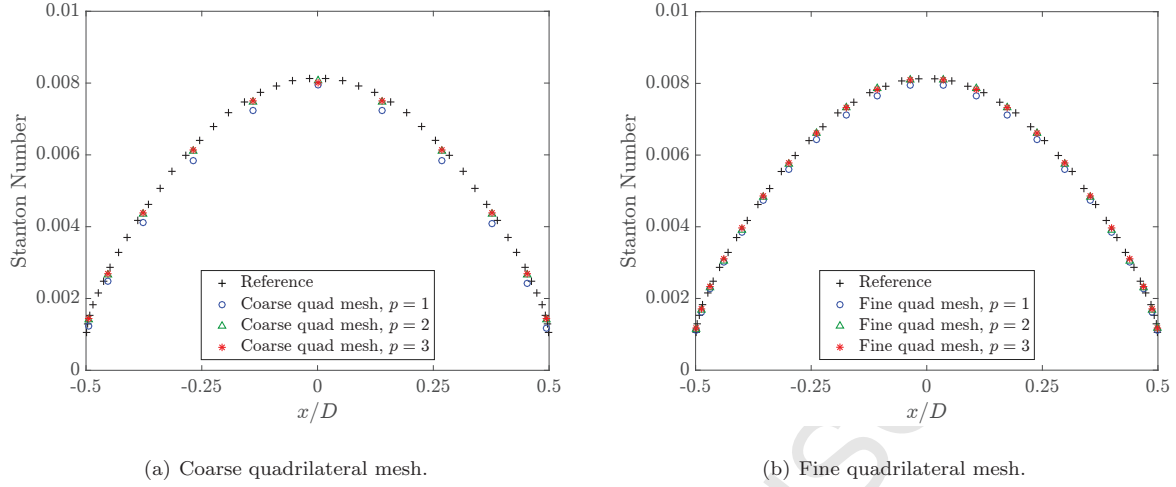


Figure 6: Heat flux profiles computed on the (a) coarse and (b) fine 2D quadrilateral meshes with $p = 1$, $p = 2$, and $p = 3$ for hypersonic flow over a circular cylinder.

Table 4: AV parameters for parametric study of effects of *magnitude* and *span* of AV on the solution to hypersonic flow over a circular cylinder.

Case	C_η	C_Δ
1	0.5	0.1
2	1.0	0.1
3	5.0	0.25
4	1.0	0.25
5	5.0	1.25

temperature distributions, shown in Figure 8. As in cases 3 and 5, an extremely large amount of AV induces significant smearing of the shock. Nevertheless, the correct post-shock state is eventually reached, albeit further downstream. Coupled with the absence of AV near the wall, the temperature distribution in the boundary layer is well captured. This results in accurate prediction of surface heat fluxes. However, in more complex flows with complicated geometries, multiple shock interactions, non-equilibrium effects, and/or shock layer radiation, excessive smearing of discontinuities could more severely corrupt the solution. For cases 2 and 4, in which the amount of AV is moderately increased, the temperature distribution is still close to that in case 1. This suggests that adding a slightly larger amount of AV than necessary is acceptable, and care must be taken only to avoid excessive dissipation.

To further examine the effects of AV on the solution, additional simulations were performed and comparisons were made among the temperature fields. Figure 9 shows the L_2 error in temperature over the

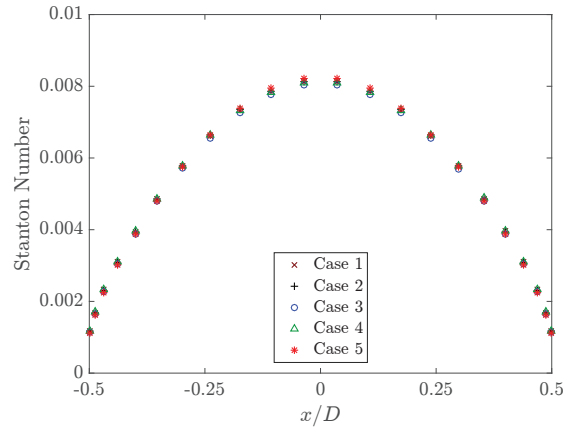


Figure 7: Heat flux profiles for hypersonic flow over a circular cylinder with different values of C_η and C_Δ , as listed in Table 4. All solutions were computed with $p = 3$ on the fine mesh.

entire domain with respect to the reference solution for all cases investigated. The white upper-left region represents the set of C_η and C_Δ that leads to an unstable solution. In general, decreasing the amount of AV decreases the error in the solution, provided a stable solution is obtainable. It can also be observed that for a fixed C_Δ , increasing C_η tends to increase the error. Lastly, a moderately sized region of low error is located in the bottom left of Figure 9. This reinforces the notion that there exists a range of AV parameters that lead to reasonable solutions and that only an excessive amount of AV must be avoided.

Furthermore, to illustrate the effects of applying the filter described in Eq. (17), Case 1 in Table 4 was calculated without applying the filter. The surface heating predictions are displayed in Figure 10. The heat flux increases substantially as a result of unnecessary AV altering the boundary layer. A significant increase in resolution in the boundary layer would be required to accurately predict surface heating. This emphasizes the importance of minimizing the amount of AV in boundary layers and only adding a small amount when necessary.

Finally, to highlight the benefits of using smooth (as opposed to elementwise-constant) AV for shock stabilization, Case 1 in Table 4 was recomputed without solving Eq. (16) to smooth the AV. Figure 11 shows the heat flux at all quadrature points on the cylinder wall in order to emphasize changes in the solution. The nonsmooth AV field induces a sharp rise in heat flux near the stagnation point, which suggests the emergence of instabilities stemming from large jumps in AV across elements. Conversely, the heat flux profile obtained with the smooth AV field is free from any spurious oscillations. Although the errors in the heat flux caused by the elementwise-constant AV are smaller than those often observed in FV solutions, this nevertheless reinforces the importance of using smooth AV fields to obtain accurate heating predictions in viscous hypersonic flows. This is consistent with a similar investigation performed by Barter and Darmofal, who solved the 1D viscous Burgers equation using smooth and nonsmooth AV fields [33].

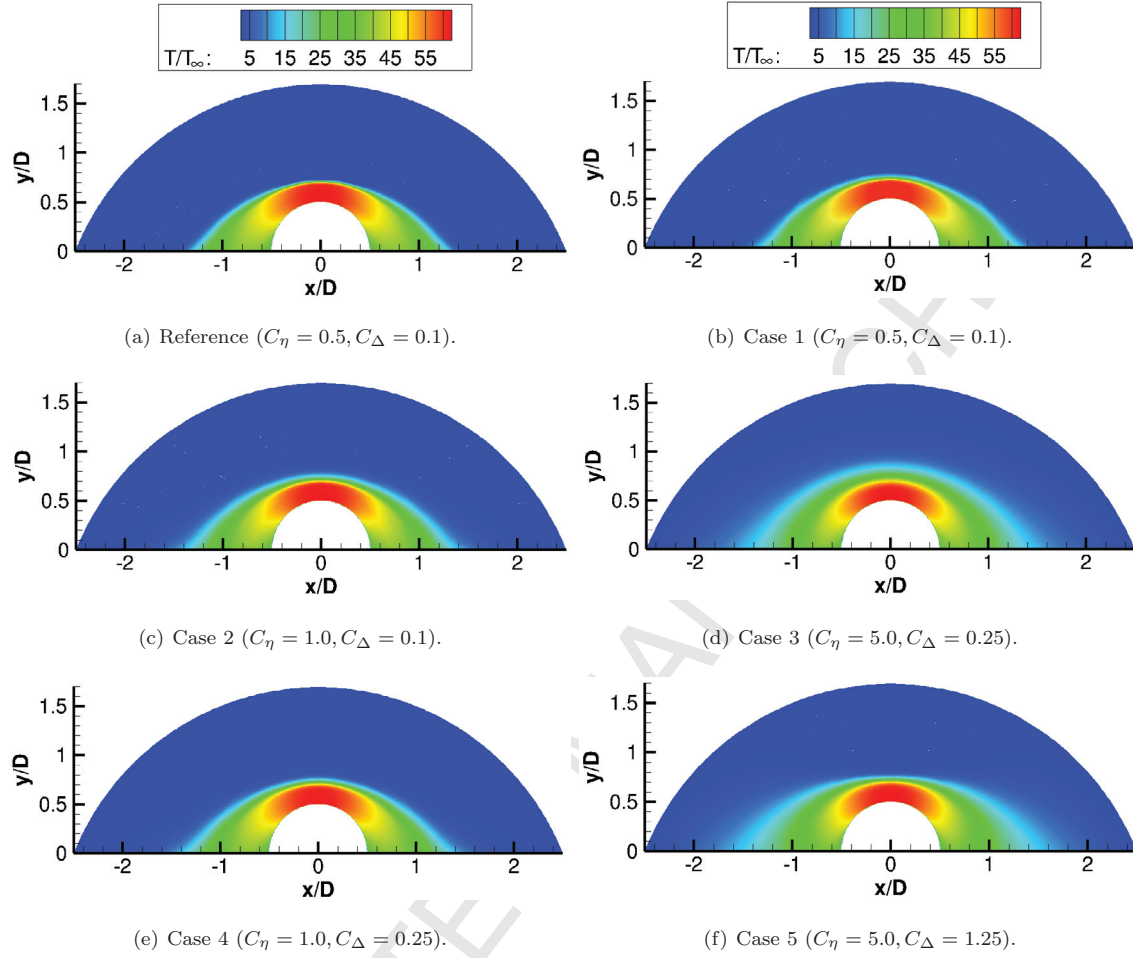


Figure 8: Temperature distributions for hypersonic flow over a circular cylinder with different values of C_η and C_Δ , as listed in Table 4. All calculations were performed with $p = 3$ on the fine mesh.

4.2.1.3 Heating prediction sensitivity to mesh topology

This section examines the sensitivity of the solution to misalignment between elements and shocks. For this, 3D tetrahedral meshes were generated from the coarse and fine quadrilateral meshes. First, each quadrilateral mesh was extruded four elements in the spanwise direction. Next, each hexahedron was partitioned into six tetrahedra by adding diagonals in a consistent manner. Table 5 provides information about the two tetrahedral meshes, which are displayed in Figure 12. The number of degrees of freedom per state variable is calculated by $N_e \times (p+1)(p+2)(p+3)/6$, where p is the polynomial order. The intentional uniform bias promotes the appearance of nonphysical asymmetries that expose deficiencies in the solution algorithm [3]. For FV calculations, this type of mesh resulted in larger asymmetries in surface heating than did a mesh

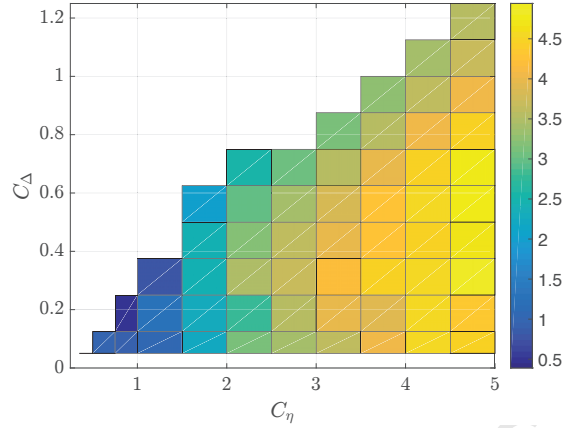


Figure 9: Normalized L_2 error in temperature, computed as $\sqrt{\int_{\Omega} (T - T_{\text{ref}})^2 d\Omega} / (T_{\infty} \sqrt{|\Omega|})$ for different values of C_{η} and C_{Δ} . T_{ref} is the temperature of the reference solution.

topology with fully unstructured tetrahedra in the shock region [3, 50, 51].

Table 5: Information regarding the tetrahedral meshes used for computing hypersonic flow over a circular cylinder. The number of degrees of freedom (per state variable for each spanwise layer of elements) is calculated by multiplying the number of elements in one spanwise layer by $(p+1)(p+2)(p+3)/6$, where p is the polynomial order.

Mesh	Element type	No. elements (per spanwise layer)	No. degrees of freedom (per spanwise layer)			Stagnation-point Stanton number ($\times 10^3$)		
			$p = 1$	$p = 2$	$p = 3$	$p = 1$	$p = 2$	$p = 3$
Coarse	Tetrahedra	1320	5280	13200	26400	7.21	7.95	8.00
Fine	Tetrahedra	5280	21120	52800	105600	7.91	8.10	8.14

The surface heat flux profiles predicted on both meshes with $p = 1$, $p = 2$, and $p = 3$ are plotted in Figure 13. For both meshes, the $p = 1$ solution exhibits evident spanwise and circumferential asymmetries in the heat flux profile as a result of the skewness in the tetrahedral elements. However, the $p = 2$ and $p = 3$ solutions achieve very good predictions of surface heating despite both the relatively large size of the elements and the strong misalignment with the bow shock. Furthermore, in spite of the fewer degrees of freedom, the coarse $p = 2$ solution is much more symmetric than the fine $p = 1$ solution. This indicates that high-order solutions are much less susceptible to errors induced by strong grid-shock misalignment than low-order solutions.

To further illuminate asymmetries, the heat fluxes for the high-order solutions are plotted at each quadrature point on the cylinder wall in Figure 14, along with a close-up view around the stagnation point. Although larger variations can indeed be observed, they are not greater than a few percent, which is signif-

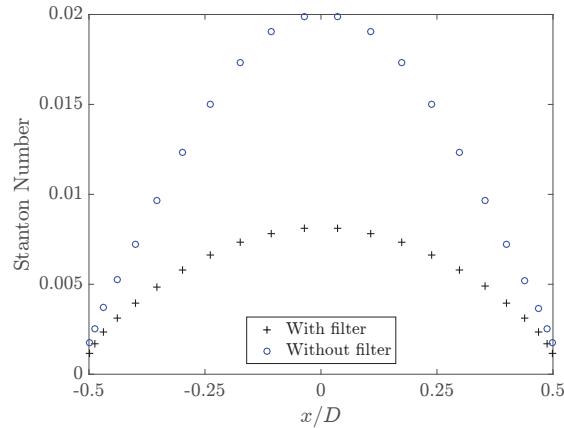


Figure 10: Heat flux profiles obtained with and without the filter in Eq. (17) for hypersonic flow over a circular cylinder. Both solutions were computed with $p = 3$ on the fine mesh using Case 1 parameters.

icantly smaller than the variations observed in FV simulations [3, 50, 51]. For the fine $p = 3$ solution, the heat flux profile is essentially perfectly symmetric.

The temperature fields for the $p = 3$ solutions on the coarse and fine meshes are displayed in Figure 15. In the coarse solution, small oscillations in the shock region are observed and the shock is slightly more smeared than in the fine solution. Nevertheless, in both cases, the shock is smoothly captured and the temperature distribution exhibits good symmetry. These results illustrate the capabilities of high-order DG calculations to accurately predict surface heating in hypersonic environments even under strong misalignment between elements and flow-field discontinuities. Emphasis is placed on the robustness of the proposed shock capturing method in capturing very strong shocks using highly skewed elements.

4.2.1.4 Heating prediction sensitivity to inviscid and viscous flux functions

The flow problem was calculated with different inviscid and viscous flux functions to assess their influence on the predicted surface heating. The inviscid flux functions examined are the Roe, HLLC, AUSM+, and SLAU Riemann solvers, while the viscous flux functions are the interior penalty (IP) [43] and BR2 schemes [38]. The AUSM+ flux function was developed by Liou [41] as an improvement over the advection upstream splitting method (AUSM). It is positivity-preserving and exactly resolves one-dimensional shocks and contact discontinuities, making it suitable for high-Mach-number flows. Similarly, the SLAU scheme is derived from the AUSM family, with special consideration for low-Mach-number regimes [42].

This parametric study was performed on the coarse quadrilateral and tetrahedral meshes with $p = 3$. The heat flux profiles obtained with the different flux functions are plotted in Figure 16. There are almost no discernible differences among the heating predictions. It should be noted, however, that the SLAU and BR2

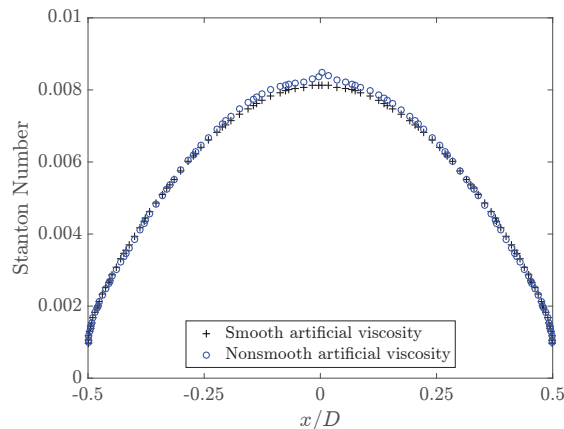


Figure 11: Heat flux profiles obtained with smooth and elementwise-constant AV fields for hypersonic flow over a circular cylinder. Both solutions were computed with $p = 3$ on the fine mesh using Case 1 parameters.

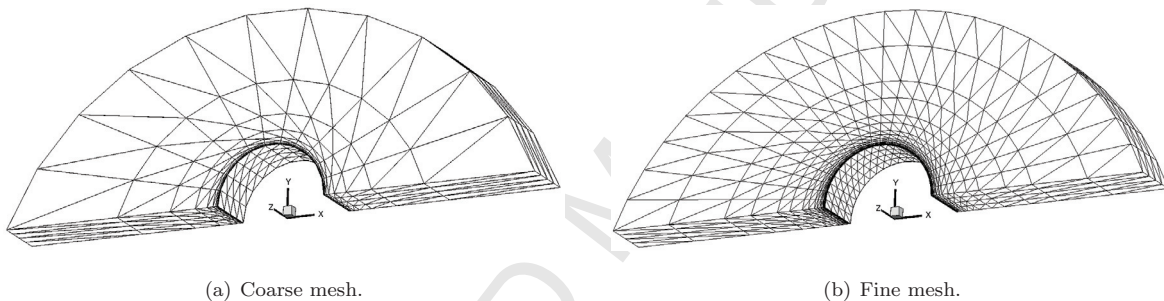


Figure 12: Tetrahedral meshes used for hypersonic flow over a circular cylinder. These meshes were generated by extruding the quadrilateral meshes, described in Table 5, and splitting the resulting hexahedra into tetrahedra.

schemes were found to give the fastest rate of residual convergence. This was confirmed in other calculations as well. The excellent agreement in the predicted heating profiles indicates a much lower sensitivity even on relatively coarse meshes to the inviscid and viscous flux functions than in FV calculations, independent of the number of spatial dimensions and element skewness [2, 5].

4.2.1.5 Error-cost comparisons with finite-volume calculations

This section presents quantitative comparisons with the Fully Unstructured Navier-Stokes 3D (FUN3D) code, a state-of-the-art node-based, fully unstructured FV solver [56, 57]. FUN3D has been applied to a variety of complex flow configurations, such as reentry vehicles, aircraft noise, and the design of flight experiments. The computation of viscous fluxes is described in [57]. For inviscid flux reconstruction, two options are available. The baseline option uses quasi-1D edge-based reconstruction based on least-squares gradient information. The second option entails multidimensional element-based reconstruction employing

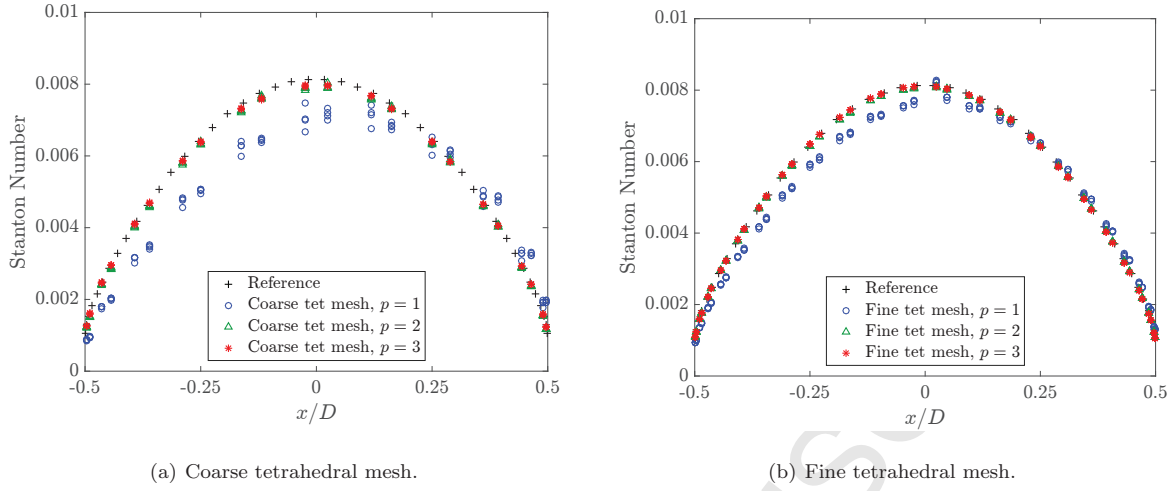


Figure 13: Heat flux profiles computed on the coarse and fine tetrahedral meshes with $p = 1$, $p = 2$, and $p = 3$ for hypersonic flow over a circular cylinder.

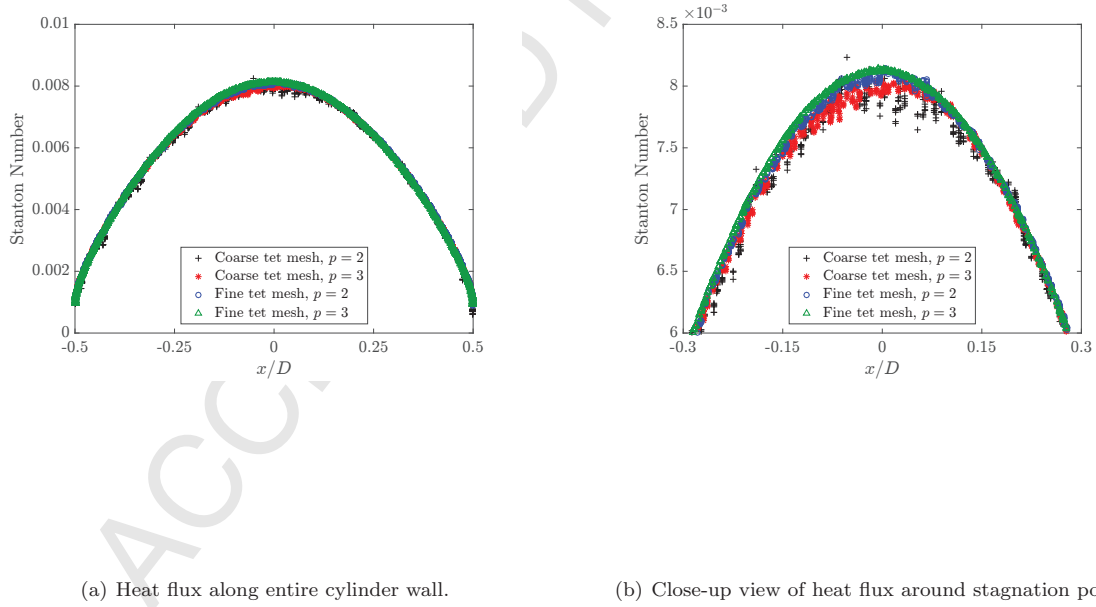


Figure 14: Heat flux at all quadrature points on the cylinder wall for the $p = 2$ and $p = 3$ solutions computed on the coarse and fine tetrahedral meshes for hypersonic flow over a circular cylinder.

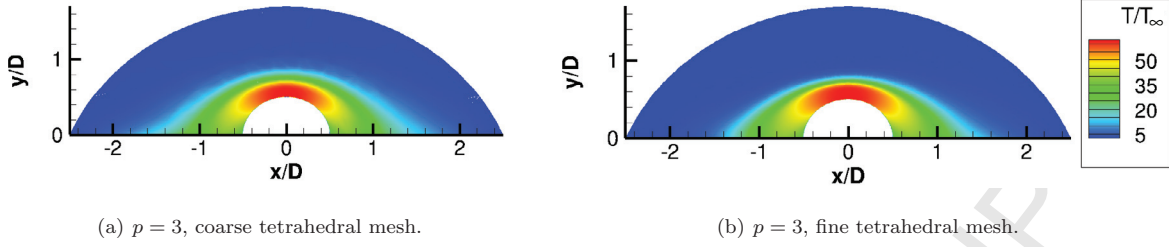


Figure 15: Temperature distributions computed with $p = 3$ on the coarse and fine tetrahedral meshes for hypersonic flow over a circular cylinder.

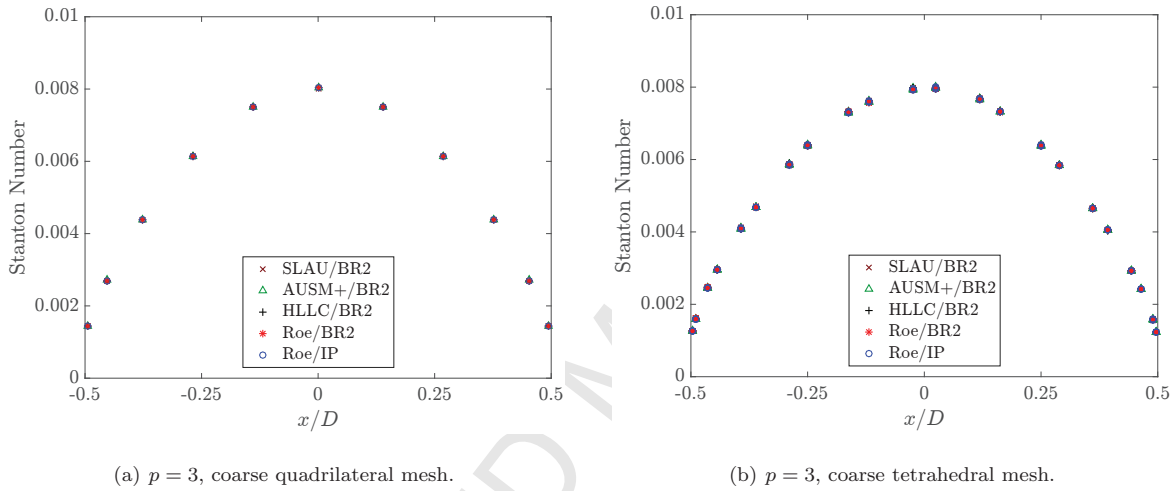


Figure 16: Heat flux profiles obtained with different flux functions for hypersonic flow over a circular cylinder. The solutions were computed using $p = 3$ on the coarse quadrilateral and tetrahedral meshes.

a Green-Gauss formulation of gradients. The multidimensional flux reconstruction algorithm was shown to provide significantly improved heating distributions on uniformly biased tetrahedral elements as compared to quasi-1D reconstruction [7]. All FUN3D results presented here were computed with second-order accuracy using the Roe flux function and a minmod limiter.

Figure 17(a) shows FUN3D results for the present flow configuration computed with quasi-1D reconstruction on three non-shock-aligned quadrilateral meshes. The coarsest FUN3D mesh is equivalent to the fine mesh described in Table 3. Given one degree of freedom per node, the total number of degrees of freedom is approximately equal to that of the $p = 1$ coarse calculation listed in Table 3. The second and third FUN3D meshes were generated from one and two uniform refinements of the coarsest mesh, respectively. A cusp in the heat flux at the stagnation point can be observed for all FV solutions. This is likely due to the eigenvalue limiting in the Roe flux function necessary for suppressing carbuncles, exacerbated by a grid that is not aligned to the captured bow shock. Here, the underresolved FV calculations overpredict the heat

flux whereas the underresolved DG calculations underpredict the heat flux. For easy visual comparison, the coarse $p = 1$ DG solution and selected high-order DG solutions with the same numbers of degrees of freedom as in the FV calculations are provided in Figure 17(b). The high-order DG solutions converge faster than the FV solutions on the given meshes.

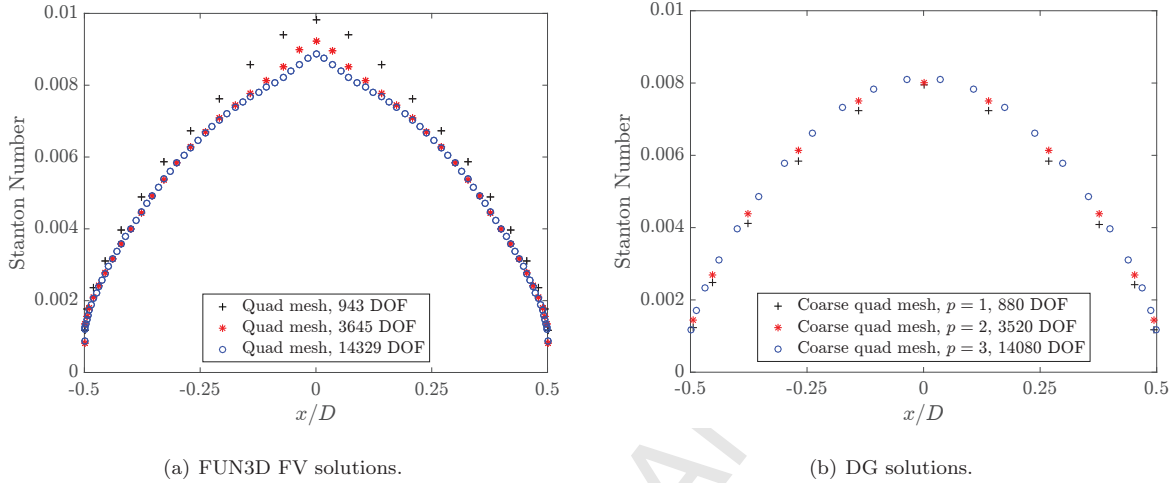


Figure 17: Comparison of heat flux profiles computed using FV and DG schemes with different numbers of degrees of freedom (DOF) for hypersonic flow over a circular cylinder. The solutions were computed on quadrilateral meshes. The DOF are given per state variable. For the FV calculations, the number of DOF is set to be the total number of nodes.

The three FUN3D quadrilateral meshes were then each extruded one element in the spanwise direction and converted into uniformly biased tetrahedral meshes by partitioning each hexahedron into six tetrahedra. Figure 18(a) displays the FV solutions computed using multidimensional flux reconstruction. The coarsest calculation exhibits very large variations in the heating profile, but consecutive mesh refinements yield improvement in the symmetry of the heat flux. For visual comparison, Figure 18(b) shows the $p = 1$, $p = 2$, and $p = 3$ DG solutions on the coarse mesh. Although asymmetries can be observed in the $p = 1$ calculation, the high-order solutions demonstrate better symmetry than the finest FV calculation with fewer degrees of freedom. These results suggest that compared to FV methods, high-order DG schemes can achieve more accurate heating predictions with fewer degrees of freedom and are much less susceptible to numerical errors caused by highly skewed elements.

4.2.2. Hypersonic flow over a sharp double cone

In the early 2000s, a blind validation study was conducted using data from hypersonic flow experiments performed in the Large Energy National Shock (LENS) wind tunnel at the Calspan-University at Buffalo Research Center (CUBRC) [58]. A number of codes employing FV formulations were benchmarked in this study. Flow over a double cone body, which is the axisymmetric analog of a double wedge, was considered.

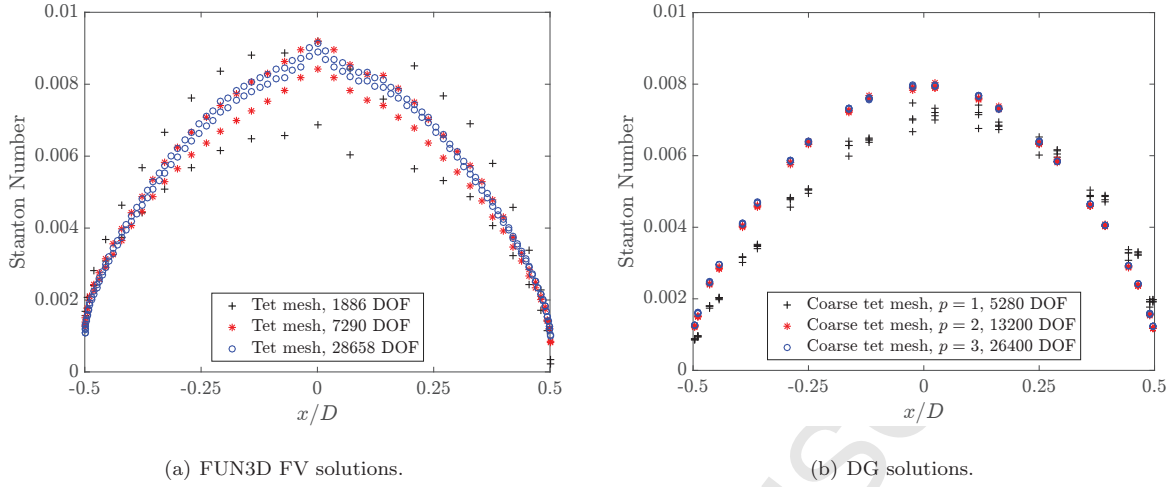


Figure 18: Comparison of heat flux profiles computed using FV and DG schemes with different numbers of degrees of freedom (DOF) for hypersonic flow over a circular cylinder. The solutions were computed on uniformly biased tetrahedral meshes. For the DG solutions, the DOF are given per state variable for each spanwise layer of elements. For the FV calculations, which used only one spanwise layer of elements, the DOF are given per state variable and set to be the total number of nodes.

The angles of the fore and aft cones are 25° and 55° , respectively. Given the finite dimensions of wind tunnel model geometries, the axisymmetry helps suppress three-dimensional features often present in experimental tests of flows that are supposedly spanwise-homogeneous. Freestream Mach numbers varied between 9.5 and 11.4 over a range of Reynolds numbers, giving rise to steady and laminar conditions. Flow separation, reattachment, free shear layers, contact discontinuities, and complex shock interactions posed difficulties for the simulations. These flow features are difficult to capture and very sensitive to both mesh resolution and solution algorithms, making for good code validation tests.

The double cone test case considered here is Run 28. The flow conditions are listed in Table 6. Despite close agreement among the FV solutions, small discrepancies with experimental results were observed, which were later attributed to the boundary conditions in the simulations. Specifically, it was found that slight flow nonuniformity, vibrational freezing of flow leaving the nozzle, and vibrational energy effects at the wall should be accounted for to obtain closer agreement with the experimental data [59]. These boundary condition corrections are not incorporated into the simulations performed in this study.

Table 6: Flow parameters for hypersonic flow over a double cone. Ma is the Mach number, Re is the unit Reynolds number, T_{wall} is the wall temperature, T_∞ is the free-stream temperature, and P_∞ is the free-stream pressure.

Ma	Re (m^{-1})	T_{wall} (K)	T_∞ (K)	P_∞ (Pa)
9.59	140,000	293.3	185.6	36.08

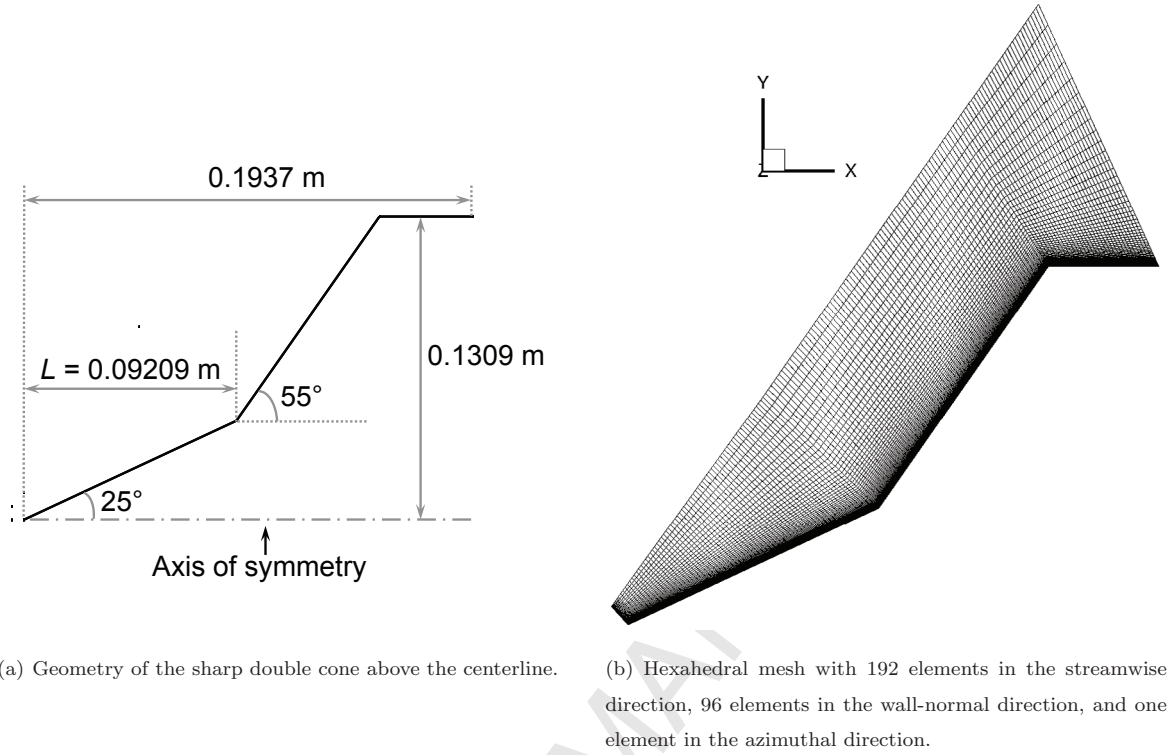


Figure 19: (a) Geometry and (b) hexahedral mesh for hypersonic flow over a double cone.

GMSH was used to create a hexahedral mesh containing 192 elements in the streamwise direction and 92 elements in the wall-normal direction. The mesh and the dimensions of the double cone body are displayed in Figure 19. The mesh was refined near the leading edge of the fore cone and near the cone surface. In addition, the mesh was extruded one degree in the azimuthal direction using one layer of elements, and to avoid a geometric singularity, the leading edge of the fore cone was slightly offset. Dirichlet boundary conditions were applied at the inflow, extrapolation was used at the outflow, and the surface was an isothermal no-slip wall. Symmetry was applied at the extruded boundaries.

A major challenge associated with the simulation of this flow is the high resolution needed to accurately capture all features of the complex flow topology, including multiple shock interactions and flow separation. Shocks of varying strengths must be detected and stabilized without the addition of excessive dissipation. In addition, due to the gradual evolution of the separation bubble, this flow takes a long time to reach steady-state conditions. Specifically, previous studies have shown that the solution must evolve for approximately one hundred characteristic flow times, defined as the ratio of the geometry length scale to the freestream velocity [4]. However, if the time step is too large, then convergence may stall and the simulation may even enter a limit cycle, failing to ever achieve steady state [60].

One notable computational issue encountered was the emergence of very sharp oscillations in the flow field at the leading edge of the fore cone. Initial meshes were not refined in the streamwise direction in this region, and AV was added to suppress these instabilities. However, even a small amount of AV smeared and shifted the leading edge of the oblique shock. This in turn caused the separation bubble, shocks, contact surfaces, and other flow features to shift upstream by approximately 15%. To resolve this issue, not only was the mesh refined in the streamwise direction in this region, but also a very small number of elements in close proximity to the fore cone leading edge were coarsened to $p = 0$. The combination of mesh refinement and p -adaptation was necessary to accurately capture the leading edge while suppressing instabilities.

The steady-state temperature and pressure fields for the $p = 3$ calculation are displayed in Figure 20, along with close-up views of regions of interest. All important flow features are well-resolved due to the high order of accuracy. The separation bubble extends from the middle of the fore cone to the middle of the aft cone. The separation-induced shock interacts with the bow shock to form a transmitted shock. A high-pressure region manifests behind the transmitted shock, downstream of which a supersonic jet emerges near the surface of the body. This is accompanied by a series of interacting and reflecting compression and expansion waves. The flow expands significantly as it passes the expansion corner.

The surface heat flux profiles for the $p = 2$ and $p = 3$ solutions are plotted in Figure 21. The numbers of degrees of freedom per state variable (in the streamwise and wall-normal directions) are 165,888 and 294,912 for the $p = 2$ and $p = 3$ calculations, respectively. No significant differences are observed between the two solutions, indicating that the $p = 2$ solution is converged. The onset of flow separation occurs at $x/L \approx 0.53$, where L is the horizontal distance between the leading edge of the fore cone and the cone-cone junction (see Fig. 19(a)). The peak Stanton number is significantly higher than in the previous test case and occurs at $x/L \approx 1.32$, downstream of which small oscillations in heating occur due to the reflected waves. As previously discussed, there are apparent discrepancies with the experimental results due to omission of vibrational nonequilibrium effects. Also included in Figure 21 is a mesh-converged FV calculation [48] on a hexahedral mesh with 1024 elements in the streamwise direction and 256 elements in the wall-normal direction computed using the Langley Aerothermodynamic Upwind Relaxation Algorithm (LAURA) code [61, 62], a structured, cell-centered flow solver suited for predicting high-enthalpy, chemically reacting nonequilibrium flows. The total number of degrees of freedom per state variable is thus 262,144, illustrating that DG calculations require fewer degrees of freedom to achieve the same level of accuracy even for a complex flow topology. Very good agreement between the DG solutions and the reference results is observed, with the DG solutions predicting the separation zone to be marginally larger and the transmitted shock location to be slightly further downstream. These results highlight the potential of employing DG methods combined with the proposed shock capturing method for realistic hypersonic applications.

This type of flow has been shown to be very sensitive to the inviscid flux function in FV simulations [60]. As such, additional $p = 2$ simulations were performed to evaluate the influence of the flux functions

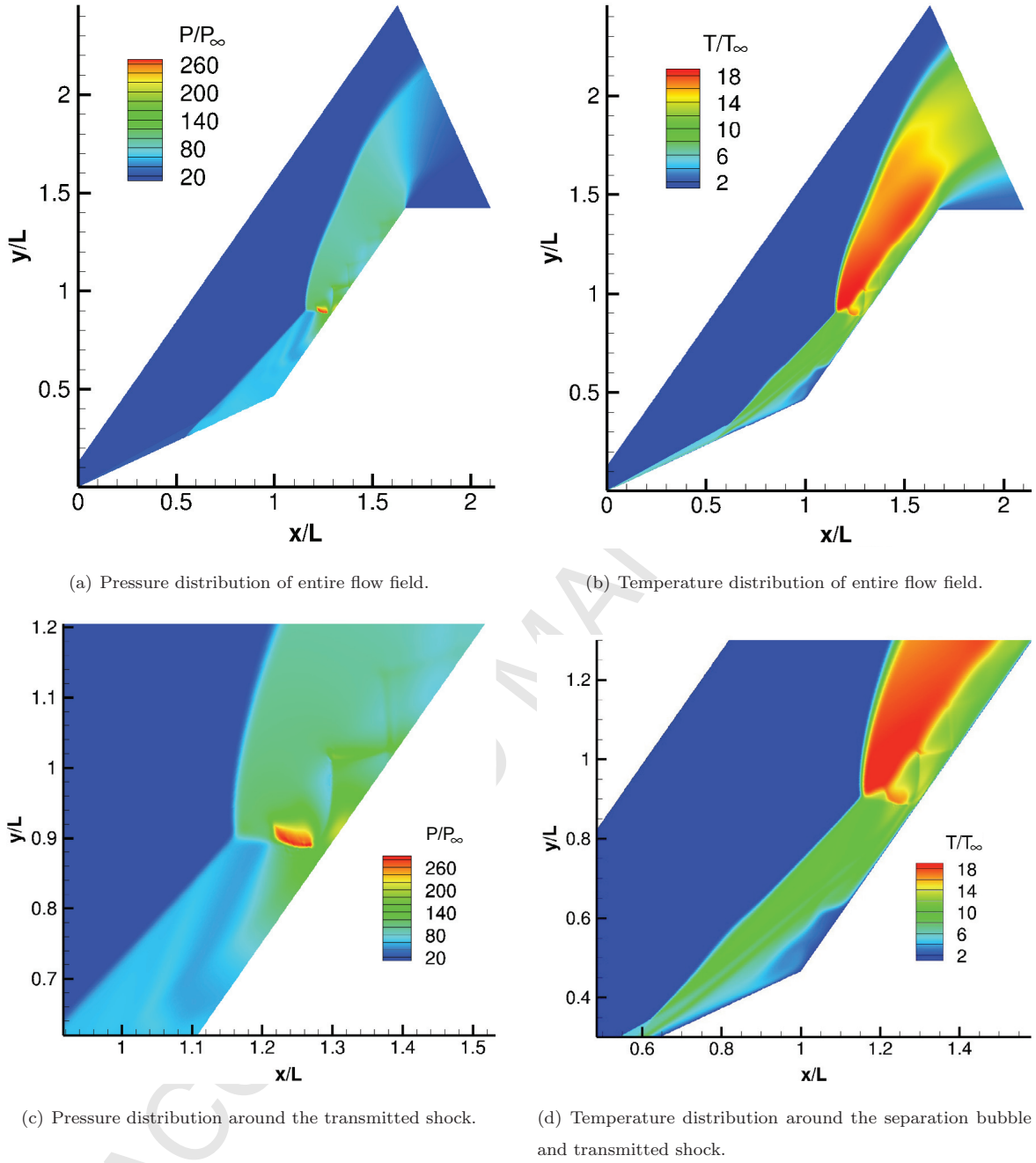


Figure 20: Pressure and temperature fields for the $p = 3$ solution of hypersonic flow over a double cone. The free-stream pressure and temperature are approximately 36.08 Pa and 185.6 K, respectively.

on the DG calculations. The resulting heat flux profiles are presented in Figure 22. Excellent agreement is observed among all calculations, reinforcing the notion that sensitivities to flux functions are very small in

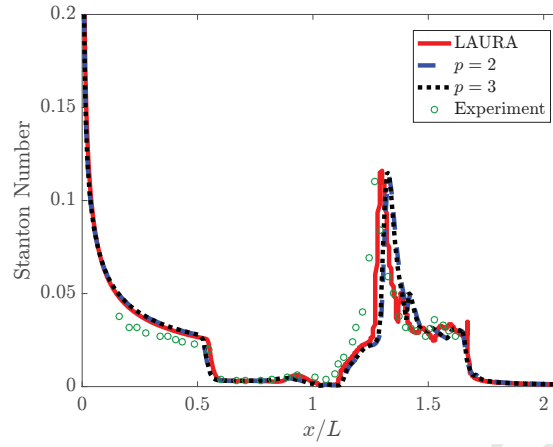


Figure 21: Surface heat flux profiles predicted by the $p = 2$ and $p = 3$ hexahedral calculations for hypersonic flow over a double cone. Experimental results [58] and a reference LAURA solution [48] are also included. $L = 0.09209$ m is the horizontal distance between the leading edge of the fore cone and the cone-cone junction.

DG simulations. Finally, to the best of the authors' knowledge, these results comprise the first high-order solutions to hypersonic flow over a double cone, or a problem of similar nature and difficulty.

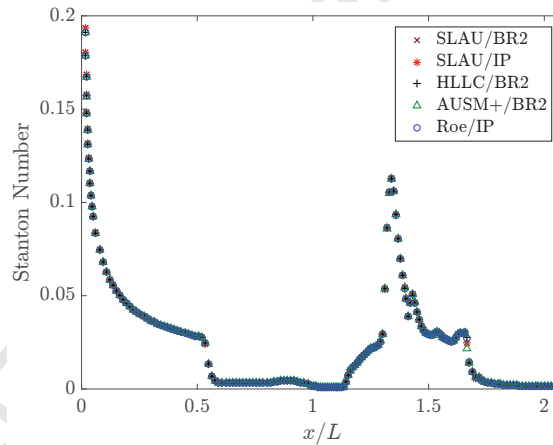


Figure 22: Surface heat flux profiles computed with different flux functions using $p = 2$ for hypersonic flow over a double cone.

5. Conclusions

This work investigated the utility of high-order DG methods for predicting heat transfer in hypersonic environments. A simple and robust shock capturing method for viscous high-speed flows was developed for DG schemes. A shock detector was formulated that employs intraelement variations to detect flow-field discontinuities, and AV is used for stabilization. The AV is smoothened by solving a time-independent linear

elliptic equation, and the amount added to boundary layers is attenuated. The shock capturing formulation was successfully employed to compute double Mach reflection and hypersonic flows over a circular half-cylinder and a double cone. The first test case is a transient inviscid flow with multiple shock interactions and fine hydrodynamic structures, the second involves a very strong bow shock and a thin boundary layer, and the final test case is characterized by flow separation, complex shock interactions, and other small-scale features.

The results gave rise to a number of findings. First, it was found that predictions of the flow field outside of boundary layers is fairly insensitive to the amount of AV added near discontinuities. Second, high-order DG methods can obtain more accurate heating predictions than low-order methods given the same number of degrees of freedom. This was confirmed in the context of DG and FV schemes. Third, even when shocks and mesh elements are strongly misaligned, high-order polynomials can accurately predict surface heat fluxes without large nonphysical oscillations. Lastly, different Riemann solvers (Roe, HLLC, AUSM+, and SLAU) and viscous flux functions (interior penalty and BR2) had almost no effect on the heating predictions. Overall, the much lower sensitivities observed in DG solutions than in FV solutions highlight the potential for computing viscous hypersonic flows with high-order DG schemes.

Acknowledgments

This work was supported by a Stanford Graduate Fellowship and a NASA Early Career Faculty grant from the NASA Space Technology Research Grants Program. Discussions with Graham Candler are gratefully acknowledged. Resources supporting this work were provided by the NASA High-End Computing (HEC) Program through the NASA Advanced Supercomputing (NAS) Division at Ames Research Center.

References

- [1] G. V. Candler, D. J. Mavriplis, and L. Trevino. Current status and future prospects for the numerical simulation of hypersonic flows. In *47th AIAA Aerospace Sciences Meeting*, Orlando, Florida, 2009. AIAA 2009-153.
- [2] K. Kitamura, E. Shima, Y. Nakamura, and P.L. Roe. Evaluation of Euler fluxes for hypersonic heating computations. *AIAA J.*, 48(4):763–776, 2010.
- [3] P. A. Gnoffo. Simulation of stagnation region heating in hypersonic flow on tetrahedral grids. In *18th AIAA Computational Fluid Dynamics Conference*, Miami, Florida, 2007. AIAA 2007-3960.
- [4] D. V. Gaitonde, P. W. Canupp, and M. S. Holden. Heat transfer predictions in a laminar hypersonic viscous/inviscid interaction. *J. Thermophys. Heat Transfer*, 16(4):481–489, 2002.
- [5] K. Kitamura. A further survey of shock capturing methods on hypersonic heating issues. In *21st AIAA Computational Fluid Dynamics Conference*, San Diego, California, 2013. AIAA 2013-2698.
- [6] K. Kitamura and Shima E. Towards shock-stable and accurate hypersonic heating computations: A new pressure flux for AUSM-family schemes. *J. Comput. Phys.*, 245:62–83, 2013.
- [7] P. A. Gnoffo. Updates to multi-dimensional flux reconstruction for hypersonic simulations on tetrahedral grids. In *48th AIAA Aerospace Sciences Meeting*, Orlando, Florida, 2010. AIAA 2010-1271.

- [8] R. Paciorri and A. Bonfiglioli. A shock-fitting technique for 2D unstructured grids. *Comput. Fluids*, 38(3):715–726, 2009.
- [9] A. Bonfiglioli, M. Grottadaurea, R. Paciorri, and F. Sabetta. An unstructured, three-dimensional, shock-fitting solver for hypersonic flows. *Comput. Fluids*, 73:162–174, 2013.
- [10] Z.J. Wang, K. Fidkowski, R. Abgrall, F. Bassi, D. Caraeni, A. Cary, H. Deconinck, R. Hartmann, K. Hillewaert, H.T. Huynh, N. Kroll, G. May, P. O. Persson, B. van Leer, and M. Visbal. High-order CFD methods: current status and perspective. *Int. J. Numer. Meth. Fluids*, 72:811–845, 2013.
- [11] B. Cockburn, G. E. Karniadakis, and C. W. Shu. The development of discontinuous Galerkin methods. In B. Cockburn, G. E. Karniadakis, and C. W. Shu, editors, *Discontinuous Galerkin Methods*, pages 3–50. Springer, Berlin, Heidelberg, 2000.
- [12] R. Hartmann and P. Houston. Adaptive discontinuous Galerkin finite element methods for the compressible Euler equations. *J. Comput. Phys.*, 183(2):508–532, 2002.
- [13] R. Hartmann, J. Held, T. Leicht, and F. Prill. Discontinuous Galerkin methods for computational aerodynamics – 3D adaptive flow simulation with the DLR PADGE code. *Aerospace Sci. Tech.*, 14(7):512–519, 2010.
- [14] Y. Lv and M. Ihme. Discontinuous Galerkin method for multicomponent chemically reacting flows and combustion. *J. Comput. Phys.*, 270:105–137, 2014.
- [15] P. Schrooyen, K. Hillewaert, T. E. Magin, and P. Chatelain. Fully implicit discontinuous Galerkin solver to study surface and volume ablation competition in atmospheric entry flows. *Int. J. Heat Mass Transfer*, 103:108–124, 2016.
- [16] F. Bassi, L. Botti, A. Colombo, A. Crivellini, N. Franchina, and A. Ghidoni. Assessment of a high-order accurate discontinuous Galerkin method for turbomachinery flows. *Int. J. Comput. Fluid Dyn.*, 30(4):307–328, 2016.
- [17] C. C. de Wiart, K. Hillewaert, E. Lorriaux, and G. Verheylewegen. Development of a discontinuous Galerkin solver for high quality wall-resolved/modelled DNS and LES of practical turbomachinery flows on fully unstructured meshes. In *ASME Turbo Expo 2015*, Montreal, Canada, 2015. Paper GT2015-43428.
- [18] C. C. de Wiart, K. Hillewaert, L. Bricteux, and G. Winckelmans. Implicit LES of free and wall-bounded turbulent flows based on the discontinuous Galerkin/symmetric interior penalty method. *Int. J. Numer. Meth. Fluids*, 78(6):335–354, 2015.
- [19] A. D. Beck, T. Bolemann, D. Flad, H. Frank, G. J. Gassner, F. Hindenlang, and C.-D. Munz. High-order discontinuous Galerkin spectral element methods for transitional and turbulent flow simulations. *Int. J. Numer. Meth. Fluids*, 76(8):522–548, 2014.
- [20] S. M. Murman, L. T. Diosady, A. Garai, and M. Ceze. A space-time discontinuous-Galerkin approach for separated flows. In *54th AIAA Aerospace Sciences Meeting*, San Diego, California, 2016. AIAA 2016-1059.
- [21] P. O. Persson and J. Peraire. Sub-cell shock capturing for discontinuous Galerkin methods. In *44th AIAA Aerospace Sciences Meeting*, Reno, Nevada, 2006. AIAA 2006-112.
- [22] M. J. Vuik and J. K. Ryan. Multiwavelet troubled-cell indicator for discontinuity detection of discontinuous Galerkin schemes. *J. Comput. Phys.*, 270:138–160, 2014.
- [23] L. Krivodonova, J. Xin, J. F. Remacle, N. Chevaugeon, and J. E. Flaherty. Shock detection and limiting with discontinuous Galerkin methods for hyperbolic conservation laws. *Appl. Numer. Math.*, 48(3):323–338, 2004.
- [24] Y. Lv, Y. C. See, and M. Ihme. An entropy-residual shock detector for solving conservation laws using high-order discontinuous Galerkin methods. *J. Comput. Phys.*, 322:448–472, 2016.
- [25] J. Qiu and C. W. Shu. A comparison of troubled-cell indicators for Runge-Kutta discontinuous Galerkin methods using weighted essentially nonoscillatory limiters. *SIAM J. Sci. Comput.*, 27(3):995–1013, 2005.
- [26] J. Yu, C. Yan, and R. Zhao. Assessment of shock capturing schemes for discontinuous Galerkin method. *Appl. Math. Mech.*, 35:1361–1374, 2014.
- [27] R. Hartmann. Adaptive discontinuous Galerkin methods with shock-capturing for the compressible Navier-Stokes equa-

- tions. *Int. J. Numer. Meth. Fluids*, 51(9-10):1131–1156, 2006.
- [28] V. Zingan, J. L. Guermond, J. Morel, and B. Popov. Implementation of the entropy viscosity method with the discontinuous Galerkin method. *Comput. Methods in Appl. Mech. Eng.*, 253:479–490, 2013.
- [29] S. Aliabadi, S. Z. Tu, and M. Watts. An alternative to limiter in discontinuous Galerkin finite element method for simulation of compressible flows. In *42nd AIAA Aerospace Sciences Meeting*, Reno, Nevada, 2004. AIAA 2004-76.
- [30] N. C. Nguyen, P. O. Persson, and J. Peraire. RANS solutions using high order discontinuous Galerkin methods. In *45th AIAA Aerospace Sciences Meeting*, Reno, Nevada, 2007. AIAA 2007-914.
- [31] A. Klöckner, T. Warburton, and J. S. Hesthaven. Viscous shock capturing in a time-explicit discontinuous Galerkin method. *Math. Model. Nat. Phenom.*, 6(3):57–83, 2011.
- [32] P. O. Persson. Shock capturing for high-order discontinuous Galerkin simulation of transient flow problems. In *21st AIAA Computational Fluid Dynamics Conference*, San Diego, California, 2013. AIAA 2013-3061.
- [33] G. E. Barter and D. L. Darmofal. Shock capturing with PDE-based artificial viscosity for DGFEM: Part I. Formulation. *J. Comput. Phys.*, 229(5):1810–1827, 2010.
- [34] N. Burgess and D. J. Mavriplis. Computing shocked flows with high-order accurate discontinuous Galerkin methods. In *42nd AIAA Fluid Dynamics Conference and Exhibit*, New Orleans, Louisiana, 2012. AIAA 2012-2715.
- [35] M. J. Brazell and D. J. Mavriplis. 3D mixed element discontinuous Galerkin with shock capturing. In *21st AIAA Computational Fluid Dynamics Conference*, San Diego, California, 2013. AIAA 2013-3064.
- [36] A. E. Papoutsakis, I. Nompelis, and J. A. Ekaterinaris. Discontinuous Galerkin discretization of chemically reacting flows. In *52nd AIAA Aerospace Sciences Meeting*, National Harbor, Maryland, 2014. AIAA 2014-0068.
- [37] P. A. Gnoffo. Planetary-entry gas dynamics. *Annu. Rev. Fluid Mech.*, 31:459–494, 1999.
- [38] F. Bassi and S. Rebay. GMRES discontinuous Galerkin solution of the compressible Navier-Stokes equations. In B. Cockburn and C. W. Shu, editors, *Discontinuous Galerkin Methods: Theory, Computation and Applications*, pages 197–208. Springer, Berlin, 2000.
- [39] P. L. Roe. Approximate Riemann solvers, parameter vectors, and difference schemes. *J. Comput. Phys.*, 43(2):357–372, 1981.
- [40] E. F. Toro, M. Spruce, and W. Speares. Restoration of the contact surface in the HLL-Riemann solver. *Shock Waves*, 4:25–34, 1994.
- [41] M. S. Liou. A sequel to AUSM: AUSM+. *J. Comput. Phys.*, 129(2):364–382, 1996.
- [42] E. Shima and K. Kitamura. Parameter-free simple low-dissipation AUSM-family scheme for all speeds. *AIAA J.*, 49(8):1693–1709, 2011.
- [43] D. N. Arnold, F. Brezzi, B. Cockburn, and L. D. Marini. Unified analysis of discontinuous Galerkin methods for elliptic problems. *SIAM J. Numer. Anal.*, 39(5):1749–1779, 2002.
- [44] M. Yano, J. M. Modisette, and D. L. Darmofal. The importance of mesh adaptation for higher-order discretizations of aerodynamic flows. In *20th AIAA Computational Fluid Dynamics Conference*, Honolulu, Hawaii, 2011. AIAA 2011-3852.
- [45] M. Yano. An optimization framework for adaptive higher-order discretizations of partial differential equations on anisotropic simplex meshes. Ph.D. Thesis, Department of Aeronautics and Astronautics, Massachusetts Institute of Technology, 2012.
- [46] M. Germano. Differential filters for the large eddy numerical simulation of turbulent flows. *Phys. Fluids*, 29(6):1755–1757, 1986.
- [47] R. W. MacCormack and G. V. Candler. The solution of the Navier-Stokes equations using Gauss-Seidel line relaxation. *Comput. Fluids*, 17(1):135–150, 1989.
- [48] P. A. Gnoffo. CFD validation studies for hypersonic flow prediction. In *39th AIAA Aerospace Sciences Meeting*, Reno, Nevada, 2001. AIAA 2001-1025.

- [49] P. Woodward and P. Collela. The numerical simulation of two-dimensional fluid flow with strong shocks. *J. Comput. Phys.*, 54(1):115–173, 1984.
- [50] I. Nompelis, T. W. Drayna, and G. V. Candler. Development of a hybrid unstructured implicit solver for the simulation of reacting flows over complex geometries. In *34th AIAA Fluid Dynamics Conference*, Portland, Oregon, 2004. AIAA 2004-2227.
- [51] P. A. Gnoffo and J. A. White. Computational aerothermodynamic simulation issues on unstructured grids. In *37th AIAA Thermophysics Conference*, Portland, Oregon, 2004. AIAA 2004-2371.
- [52] P. A. Gnoffo. Multi-dimensional, inviscid flux reconstruction for simulation of hypersonic heating on tetrahedral grids. In *47th AIAA Aerospace Sciences Meeting*, Orlando, Florida, 2009. AIAA 2009-599.
- [53] B. van Leer. Towards the ultimate conservative difference scheme. V. A second-order sequel to Godunov’s method. *J. Comput. Phys.*, 32(1):101–136, 1979.
- [54] G. D. van Albada, B. van Leer, and W. W. Roberts Jr. A comparative study of computational methods in cosmic gas dynamics. *Astron. Astrophys.*, 108:76–84, 1982.
- [55] C. Geuzaine and J. F. Remacle. Gmsh: A 3-D finite element mesh generator with built-in pre- and post-processing facilities. *Int. J. Numer. Meth. Eng.*, 79(11):1309–1331, 2009.
- [56] R. T. Biedron, J.-R. Carlson, J. M. Derlaga, P. A. Gnoffo, D. P. Hammond, W. T. Jones, B. Kleb, E. M. Lee-Rausch, E. J. Nielsen, M. A. Park, C. L. Rumsey, J. L. Thomas, and W. A. Wood. FUN3D manual: 13.1. NASA Langley Research Center, NASA TM-2017-219580, Hampton, Virginia, 2017, 2017.
- [57] W. K. Anderson and D. L. Bonhaus. An implicit upwind algorithm for computing turbulent flows on unstructured grids. *Comput. Fluids*, 23(1):1–21, 1994.
- [58] J. K. Harvey, M. S. Holden, and T. P. Wadhams. Code validation study of laminar shock/boundary layer and shock/shock interactions in hypersonic flow; Part B: Comparison with Navier-Stokes and DSMC solutions. In *39th AIAA Aerospace Sciences Meeting*, Reno, Nevada, 2001. AIAA 2001-1031.
- [59] I. Nompelis, G. V. Candler, and M. Holden. Effect of vibrational nonequilibrium on hypersonic double-cone experiments. *AIAA J.*, 41(11):2162–2169, 2003.
- [60] I. Nompelis. Computational study of hypersonic double-cone experiments for code validation. Ph.D. Thesis, University of Minnesota, 2004.
- [61] A. Mazaheri, P. A. Gnoffo, C. O. Johnston, and B. Kleb. LAURA users manual: 5.5-65135. NASA Langley Research Center, NASA TM-2013-217800, Hampton, Virginia, 2013.
- [62] P. A. Gnoffo, R. N. Gupta, and J. L. Shinn. Conservation equations and physical models for hypersonic air flows in thermal and chemical nonequilibrium. NASA TP-2867, 1989.